



저작자표시-비영리-변경금지 2.0 대한민국

이용자는 아래의 조건을 따르는 경우에 한하여 자유롭게

- 이 저작물을 복제, 배포, 전송, 전시, 공연 및 방송할 수 있습니다.

다음과 같은 조건을 따라야 합니다:



저작자표시. 귀하는 원저작자를 표시하여야 합니다.



비영리. 귀하는 이 저작물을 영리 목적으로 이용할 수 없습니다.



변경금지. 귀하는 이 저작물을 개작, 변형 또는 가공할 수 없습니다.

- 귀하는, 이 저작물의 재이용이나 배포의 경우, 이 저작물에 적용된 이용허락조건을 명확하게 나타내어야 합니다.
- 저작권자로부터 별도의 허가를 받으면 이러한 조건들은 적용되지 않습니다.

저작권법에 따른 이용자의 권리는 위의 내용에 의하여 영향을 받지 않습니다.

이것은 [이용허락규약\(Legal Code\)](#)을 이해하기 쉽게 요약한 것입니다.

[Disclaimer](#)

MASTER'S THESIS OF NATURAL SCIENCE

**Experimental Investigation of Thermal Dispersion
under Forced Groundwater Flow through Lab-Scale
Tests to Design an Optimal GWHP System**

개방형 지열시스템 내 교란된 지하수 환경에서의 열분산
특성 파악을 위한 실험적 연구

August 2016

**Graduate School of Seoul National University
College of Natural Science
School of Earth and Environmental Sciences**

Lee, Bo-Hyun

ABSTRACT

Due to the direct use of groundwater as a heat source/sink, the efficiency of GWHP system depends on hydrological and thermal properties of the aquifer in a complex manner. Although a few studies have been conducted to identify key factors affecting the performance of the system, most of them did not focus on thermal properties but flow conditions and well arrangement. However, thermal dispersion was recently recognized for its significance in the high flow field which can be commonly induced by GWHP systems. Therefore, it is needed to further research on how thermal dispersion affects the heat transport in GWHP systems. In this research, a laboratory device simulating the heat transport in saturated porous medium was designed to investigate thermal dispersion behavior under forced groundwater flow conditions. The main goal of this study is to compare the thermal dispersion coefficient in forced flow environments with that in natural flow environments through lab-scale heat tracer tests and further simulations using two different heat sources: (a) a resistor and (b) water injection. The longitudinal/transverse thermal dispersion coefficients under natural flow condition were derived from the tests with a resistor. A linear dependency of the coefficients on flow velocity was examined in this study probably due to the flow conditions being limited to conduction-dominated flow environment ($Pe^t < 1$). Thermal dispersion coefficients computed from numerical simulations using the model validated with water-injection tests showed higher values because of the disturbance in flow velocity field. The increase of thermal dispersion coefficients compared to the natural flow condition (without-injection) became larger in the lower regional flow velocity with the higher injection rate. This implicate that the influence of thermal dispersion in navigating thermal plume movement can be significant in the forced flow field,

especially when the groundwater flow is slow and the operated injection rate is high. Therefore, it is important to give careful consideration to the adoption of thermal dispersion value when assessing the heat transport with water injection. Otherwise, the oversight of thermal dispersion term may cause a critical error in predicting thermal plume movement in forced flow fields.

Key words: groundwater heat pump (GWHP) system, forced groundwater flow, water injection, heat tracer test, thermal dispersion coefficient, flow velocity

LIST OF CONTENTS

ABSTRACT	i
LIST OF CONTENTS	iii
LIST OF FIGURES	iv
LIST OF TABLES	ix
1 INTRODUCTION	1
1.1 Background	1
1.2 Objectives	5
2 LITERATURE REVIEW	6
2.1 Groundwater Heat Pump (GWHP) system	6
2.2 Heat transport theory	9
3 METHODS AND MATERIALS	15
3.1 Laboratory experiment.....	15
3.2 Estimation of thermal dispersion	41
4 RESULTS AND DISCUSSIONS	55
4.1 Heat tracer tests using a resistor without regional groundwater flow.....	55
4.2 Heat tracer tests using a resistor under various flow conditions.....	61
4.3 Heat tracer tests with water injection under various flow conditions.....	72
4.4 Discussions.....	84
5 CONCLUSION	91
6 REFERENCES	93

LIST OF FIGURES

Fig. 1-1. Schematic diagram of (a) closed-loop GSHP system (GCHP) and (b) open-loop GSHP system (GWHP)	4
Fig. 2-1. Use of GWHP system in (a) summer (groundwater: heat sink) and (b) winter (groundwater: heat source)	8
Fig. 2-2. Results of previous researches on the relationship between the thermal dispersion and the flow velocity	14
Fig. 3-1. A rectangular acryl glass sand tank (1.3 m x 0.6 m x 0.8 m) supported by manually assembled Aluminum frame (a, b) and fine wire mesh attached on the acryl glass plates between three chambers (c).....	17
Fig. 3-2. An acrylic pipe of ϕ 14 mm (i.d.) and 0.7 m length with 0.02 m-wide screen at 0.3 m-height from the bottom(a) and acrylic tubes of ϕ 8 mm (i.d.) and 0.7 m length used to fix the RTD sensors at the planned locations (b).....	18
Fig. 3-3. A schematic design of the laboratory experimental system in (a) a front view and (b) a plan view: locations of a resistor (sky-blue star), a well pipe (red star) and RTD sensors (black and blue dots).....	19
Fig. 3-4. Well system compositions: (a) a peristaltic pump and PVC tubings (GILSON) and (b) a thermostatic barrel equipped with heaters inside....	21
Fig. 3-5. Flow rates chart with different PVC tubing sizes (in diameter) and RPMs of the peristaltic pump with (a) a high flow pump-head and (b) a standard flow pump-head.....	22
Fig. 3-6. Instruments for heat excitement: (a) a wire-wound resistor and (b) DC power supply, and measurement devices: (c) RTD sensors (Pt 100), (d) NI modules (NI 9217), and (e) eight-slot chassis (NI compact DAQ 9178).....	25
Fig. 3-7. A Setting for the performance test of a wire-wound resistor with the	

<p>established DAQ system to examine the energy transfer efficiency: (a) an insulated beaker filled with tap water and equipped with a resistor and a RTD sensor, (b) a stirrer, (c) DC power supply, (d) DAQ devices, and (e) the LabVIEW program.....</p>	26
<p>Fig. 3-8. Result of the performance test. Only one data point (blue square) every 30 seconds is shown on the graph and the linear regression curve (red line) indicates constant energy supply from the resistor</p>	27
<p>Fig. 3-9. Diagram showing the composition and the mechanism of DAQ (Data Acquisition) system.....</p>	30
<p>Fig. 3-10. LabVIEW program designed to acquire temperature data from RTD sensors: (a) the structure of the block diagram and (b) the corresponding objects on the front panel.....</p>	31
<p>Fig. 3-11. Fundamental analyses to measure physical properties of the sand materials: (a and b) grain size analysis, (c) constant-head permeameter test, and (d) porosity measurement.....</p>	35
<p>Fig. 3-12. Result of grain size analyses showing the grain size distribution.....</p>	36
<p>Fig. 3-13. Arrangement of heat sources and sensors (above). Step-wise wet packing of sand materials (below)</p>	38
<p>Fig. 3-14. Locations of Heat sources (resistor: red circle, injection point: blue circle) and RTD sensors on the X-Y plane at the height of 0.3 m (z-axis) from the bottom. Actual location of the resistor (0.4, 0.3, 0.3) was considered as a standard point (0, 0, 0) in the analytical approach.....</p>	39
<p>Fig. 3-15. Insulation of experimental device (left) and finishing work of experimental setup with DAQ system connection (right)</p>	40
<p>Fig. 3-16. Model domain and boundary conditions for 2-D heat transport simulation</p>	47
<p>Fig. 3-17. Results of preliminary 2-D heat transport simulations using FEFLOW under different flow velocities.....</p>	48
<p>Fig. 3-18. Spatial discretization of the 3-D model domain.....</p>	49

Fig. 3-19. Determination of temporal discretization in 3-D heat transport simulation	50
Fig. 3-20. Schematic model domain (in x-y plan view) and boundary conditions for 3-D heat transport simulation	51
Fig. 4-1. Concept of the heat tracer test without regional flow and the heat transfer process only related to heat conduction.....	57
Fig. 4-2. The temperature breakthrough curves obtained by the measurement (in cross-shape symbol) and the CPS model results (in a solid line) for the first experiment. RTDs on the center line (in a red color) is located along the x-axis away from the heat source. The distance(r) from the heat source was computed when the best fit was met.	58
Fig. 4-3. The temperature breakthrough curves obtained by the measurement (in cross-shape symbol) and the CPS model results (in a solid line) for the repeated experiment	59
Fig. 4-4. Concept of the heat tracer test with regional flow and the heat transfer process based on heat dispersion and heat convection.....	63
Fig. 4-5. The temperature breakthrough curves obtained by the measurements on center-line (in a cross-shape symbol) and the MCPS model results (in a solid line): (a) flow condition of $q = 1.96$ m/d and (b) flow condition of $q = 3.21$ m/d.....	64
Fig. 4-6. The temperature breakthrough curves obtained by the measurements on center-line (in a cross-shape symbol) and the MCPS model results (in a solid line): (a) flow condition of $q = 5.46$ m/d and (b) flow condition of $q = 6.96$ m/d.....	65
Fig. 4-7. The temperature breakthrough curves obtained by the measurements on center-line (in a cross-shape symbol) and the MCPS model results (in a solid line): (a) flow condition of $q = 14.43$ m/d and (b) flow condition of $q = 19.46$ m/d.....	

.....	66
Fig. 4-8. The temperature breakthrough curves obtained by the measurements on center-line (in a cross-shape symbol) and the MCPS model results (in a solid line): (a) flow condition of $q = 21.78$ m/d and (b) flow condition of $q = 23.62$ m/d.....	67
Fig. 4-9. The temperature breakthrough curves obtained by the measurements on center-line (in a cross-shape symbol) and the MCPS model results (in a solid line): (a) flow condition of $q = 25.44$ m/d and (b) flow condition of $q = 26.14$ m/d.....	68
Fig. 4-10. The result of regression analyses for longitudinal thermal dispersion coefficients ($D_{L,t}$) and thermal front velocities (v^t) in this experiment. Linear increasing trend of $D_{L,t}$ with v^t (in a blue solid line) shows R^2 of 0.7176. Non-linear increasing trend of $D_{L,t}$ with v^t (in a red solid line) shows R^2 of 0.6212.	70
Fig. 4-11. The result of regression analyses for transverse thermal dispersion coefficients ($D_{T,t}$) and thermal front velocities (v^t) in this experiment. Linear increasing trend of $D_{T,t}$ with v^t (in a blue solid line) shows R^2 of 0.4934 Non-linear increasing trend of $D_{T,t}$ with v^t (in a red solid line) shows R^2 of 0.4870.	71
Fig. 4-12. Comparison of the temperature data obtained from the numerical simulation (in triangle) with that from the experiment (in x-shape) at observation points ($r = 0.10$ and 0.15 m): (a) heat tracer test under $q = 3.21$ m/d and $Q_{water} = 70$ ml/min, (b) heat tracer test under $q = 6.96$ m/d and $Q_{water} = 70$ ml/min.....	75
Fig. 4-13. The temperature response data at $x_{obs} = 0.45$ m ($x_{inj} = 0.35$ m) obtained from heat tracer test simulations with (in a green symbol) and without (in a red symbol) water injection under (a) lowest flow condition (case A) and (b) highest flow condition (case F)	79
Fig. 4-14. NRMSE between temperature data resulted from simulation with and	

without water injection for all 24 cases obtained at 3 observation points: (a) $x_{obs} = 0.45$ m, (b) $x_{obs} = 0.50$ m, (c) $x_{obs} = 0.55$ m ($x_{inj} = 0.35$ m).....	80
Fig. 4-15. Flow velocity field along the center-line ($x = 0\sim 1$ m, $y = 0.3$ m, $z = 0.3$ m) depending on the injection rate in simulation case B.....	81
Fig. 4-16. The ratio (or degree) of flow velocity increase (or disturbance) at three observation points (a-c) for 24 cases	82
Fig. 4-17. The ratio of change in longitudinal (above) and transverse (below) thermal dispersion coefficients arisen from the disturbed flow velocity field by injection for 24 cases	83
Fig. 4-18. Comparison between non-linear increasing trend resulted from this study and one resulted from Rau et al. (2012). The flow conditions were limited below $Pet = 1$ in this study.	87
Fig. 4-19. Temperature breakthrough curves obtained from case A-1 simulations with different ($x1$, $x10$, and $x100$) thermal dispersivities ($\beta_{L/T}$). The observation point was one located at $x = 0.45$ m; $r_{inj-obs} = 0.10$ m.....	90

LIST OF TABLES

Table 3-1. Measured physical properties of porous medium (packed sand).....	37
Table 3-2. Hydrogeological and thermal parameters used for 2-D model simulation	46
Table 3-3. Hydrogeological and thermal parameters used for 3-D model simulation	52
Table 4-1. Thermal properties of porous medium and sensor location derived from the best fit between measurements and the model.....	60
Table 4-2. Thermal dispersion coefficients and thermal front velocity derived from the best fit between measurements and the model.....	69
Table 4-3. Thermal properties used in numerical simulations (other design parameters: pre-determined in section 3.2.2)	74
Table 4-4 Case simulations with different hydraulic gradient (or flow velocity) and injection rate.....	78

1 Introduction

1.1 Background

The Ground Source Heat Pump (GSHP) system is a space heating and cooling system which uses the ground or groundwater as a heat source in the winter and as a heat sink in the summer because the temperature at a few meters below the earth's surface remains relatively constant (Fig. 1-1). As it reduces CO₂ emission and yet has higher system efficiency than conventional air-source heat pump system, installation of the GSHP system has increased in recent years in Korea (Kwon et al., 2012). However, high efficiency of the GSHP system may not be easily achieved everywhere since the system efficiency significantly depends on hydrogeological characteristics of aquifers (Lo Russo, 2011; Nam and Ooka, 2010).

In closed-loop GSHP systems which extract/release the heat energy from/to the subsurface through the circulation of carrier fluid in a closed pipe, the thermal conductivity of the porous medium has a great effect on performance of the system. Thus, thermal response tests have been widely performed to estimate the thermal conductivity before designing closed-loop system. On the other hand, in open-loop systems or Groundwater Heat Pump (GWHP) systems where thermal exchange occurs directly on the pumped groundwater and the water is generally re-injected, heat transfer is mostly convective and dispersive. Since hydrologic and thermal properties of aquifers influence the performance of GWHP systems in a complex way, it has not been easy to accurately predict groundwater and heat transfer depending on aquifer characteristics (Cassaso and Sethi, 2014; Nam and Ooka 2010; Park et al., 2015).

Although a few studies have been conducted recently to investigate factors that

significantly affects the performance of GWHP systems and to design efficient systems, most of them have been focused on groundwater flow conditions (e.g. flow direction and velocity) and well placement (Gao et al., 2013; Lo Russo et al., 2011; Nam and Ooka, 2010; Zhou et al., 2013). However, as Lo Russo and Civita (2011) and Park et al. (2015) claimed in their researches, evolution of thermal plume from an injection well which may lead to a thermal breakthrough toward the pumping well and therefore degrade the system performance can considerably depend on thermal properties such as thermal dispersivity. It is needed to further investigate how the heat transport process depends on thermal characteristics of aquifers in GWHP systems.

It is known that among thermal properties of aquifers, thermal dispersion shows a greater impact on heat transport mechanism with increasing flow velocities (De Marsily, 1986; Green et al., 1964; Levec and Carbonell, 1985; Metzger et al., 2004; Rau et al., 2012). Because GWHP systems force higher flow field upon natural groundwater flow field by pumping and injecting groundwater, thermal dispersion will have a great influence on the heat transport in the system (Park et al., 2015). As solute dispersion can be identified by solute tracer tests, thermal dispersion can be estimated by heat tracer tests where the heat is induced by certain type of heat source and the temperature is monitored around the source during the experimental run. While thermal tracer tests in the field is subject to the heterogeneity of hydraulic and thermal properties of aquifers, laboratory experiments have advantages in focusing only on parameters of interests by controlling other aquifer properties and boundary conditions. Lab-scale heat tracer tests can increase the accuracy in estimating thermal dispersion compared to field experiments.

Even though laboratory experiments investigating the significance and the

magnitude of thermal dispersion in porous media has been conducted in a last few decades, most of them supplied heat by a probe or a line type resistor and adjusted water flow by hydraulic head difference to study thermal dispersion behavior within the natural groundwater flow condition (Green et al., 1964; Levec and Carbonell, 1985; Metzger et al., 2004; Rau et al., 2012, 2014). Laboratory tests that used injection of warmed water to investigate thermal dispersion behavior under high or forced groundwater flow which can commonly occur in a GWHP system were rare. Therefore, an experimental investigation of thermal dispersion through lab-scale tests with heated water injection will not only expand the scope of experimental research on thermal dispersion behavior but also bring a hydrogeological point of view into geothermal engineering field so that heat transport in GWHP systems can be studied more thoroughly.

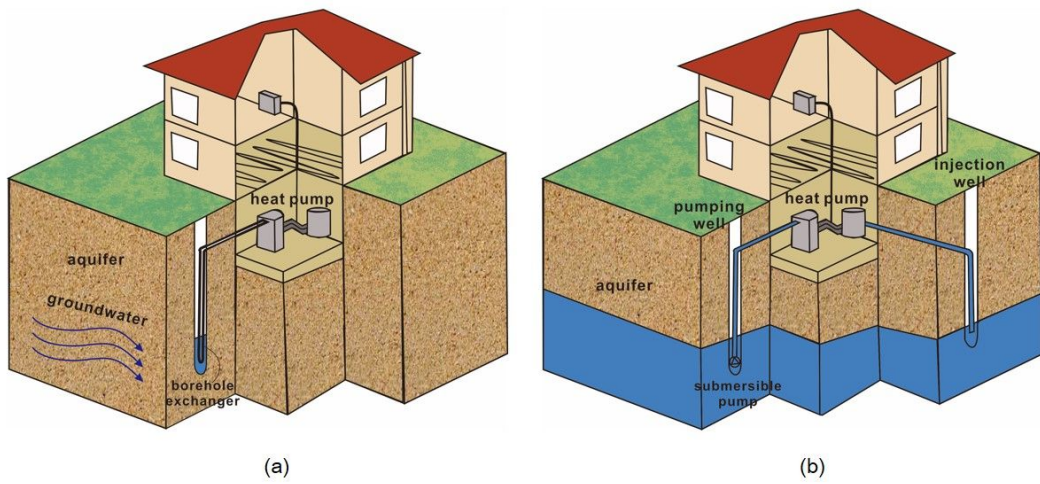


Fig. 1-1. Schematic diagram of (a) closed-loop GSHP system (GCHP) and (b) open-loop GSHP system (GWHP) (modified from Cassaso and Sethi, 2014).

1.2 Objectives

In this research, a laboratory device which mainly consists of a sand tank with a resistor and an injection well was designed to simulate the heat transfer both in natural groundwater flow field and in forced groundwater flow field. The device was used to perform heat tracer tests so that the heat transport process under both natural flow field and forced flow field can be characterized and the respective thermal dispersion coefficient can be compared.

First, heat tracer tests using a small resistor as a point heat source were conducted with different flow velocities within the natural groundwater flow range. The estimated thermal dispersion coefficients through analytical modeling approach were used to examine the debatable velocity dependence of thermal coefficient in the study field. Furthermore, they were compared with the values resulted from heat tracer tests under the forced groundwater flow condition.

Then, heated water was injected through a well pipe as a point heat source while inducing a high flow field superposed on the natural groundwater flow. The experimental results were used to validate a numerical model which enabled fair comparison between the heat transport in natural and forced flow environments through simulations. The results from numerical simulations of heat tracer tests with warm water injection were used to assess the difference in thermal dispersion coefficient under forced flow compared to natural flow. In addition, the influence of the regional flow velocity and the injection rate on the change in thermal dispersion coefficients under forced flow was studied.

2 Literature reviews

2.1 Groundwater Heat Pump (GWHP) system

Groundwater Heat Pump (GWHP) system is an open-loop GSHP system that draws groundwater from a well which has relatively stable temperature through the year, exchange heat energy with the water and discharge it through the other well (Fig. 2-1). While closed-loop systems mainly depend on the conductive heat transport, the heat transport that affects the performance of GWHP systems is mostly convective and dispersive (Cassaso and Sethi, 2014; Park et al., 2015). For this reason, GWHP system efficiency depends on hydrologic and thermal properties of the aquifer in a complex manner, which makes it difficult to design an efficient and stable GWHP system (Cassaso and Sethi, 2014; Nam and Ooka, 2010; Park et al., 2015).

In recent years, a group of authors have been trying to assess thermal risks that could deteriorate the efficiency of GWHP systems and evaluate the influence of aquifer properties on heat flow to design an efficient and sustainable GWHP system. David Banks (2009) proposed a general stepwise assessment of thermal risk that a plume of cooled or warmed groundwater returns back from the injection well to the pumping well and gradually degrade the performance of GWHP system. For simplicity, his approach was mainly based on the well separation, yield and hydrogeological conditions excluding dispersion effects and thermal properties. Nam and Ooka (2010) conducted 3D numerical simulation of groundwater and heat transport and field experiments to develop the optimum design for GWHP system. They suggested that groundwater flow conditions and well position should be taken into account when designing a GWHP system. Zhou et al. (2013) conducted a heat-water transfer

numerical simulation and laboratory experiment to study the evolution of aquifer temperature field depending on the groundwater flow field. Their results showed that the direction and velocity of groundwater flow should be taken into account to design a GWHP system. While Gao et al. (2013) performed the experiment and the numerical modelling by using the same experimental device in Zhou et al. (2013), they focused on the influence of well arrangement on the energy efficiency of multi-well GWHP system. They concluded that the row-type arrangement of well groups for pumping and injecting may be a better choice to minimize thermal breakthrough intensity and enhance the system efficiency.

Most of the previous studies on efficient GWHP system design have focused on groundwater flow condition and well placement. However, recent studies confirmed that the evolution of thermal plume significantly depends on thermal properties of aquifers, especially thermal dispersivity (Lo Russo, 2008; Lo Russo and Civita, 2009; Park et al., 2015). Park et al. (2015) showed that the thermal dispersivity had a great effect both on the temperature distribution and the extent of thermal plume in the field experiments they performed.

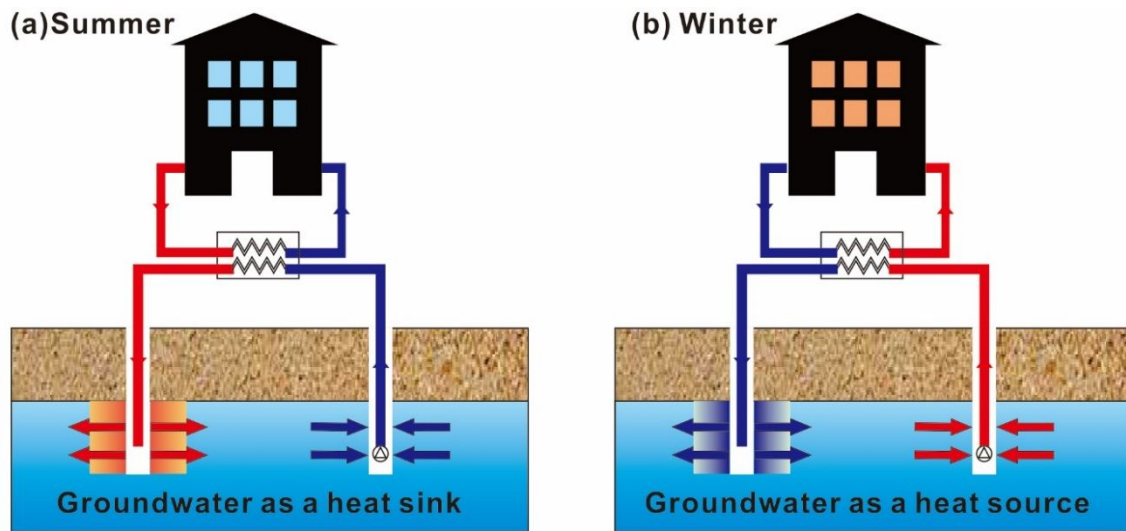


Fig. 2-1. Use of GWHP system in (a) summer (groundwater: heat sink) and (b) winter (groundwater: heat source).

2.2 Heat transport theory

2.2.1 Heat transport equation

Assuming there is no temperature difference between solid and liquid, which is called assumption of local thermal equilibrium, heat transfer in the saturated porous media is characterized by two mechanisms: (i) a convection phenomenon and (ii) a dispersion phenomenon which combines (a) a pure conduction in two phases, solid plus liquid, and (b) mechanical dispersion caused by variable velocities in pore scale and the heterogeneity of velocity field in macroscopic scale (De Marsily, 1986; Levec and Carbonell, 1985; Stauffer et al., 2014).

The principle of energy conservation makes it possible to describe heat transfer in the saturated porous media through a differential heat transport equation (HTE) that takes into account both convective and dispersive transport (De Marsily, 1986; Rau et al., 2012),

$$D^t \nabla^2 T - v^t \cdot \nabla T = \frac{\partial T}{\partial t} \quad (\text{Eq.2-1})$$

where T [$^{\circ}\text{C}$] is the temperature of the porous medium, D^t [m^2s^{-1}] represents the thermal dispersion coefficient which consists of the thermal diffusion and the thermal dispersion terms, and v^t [ms^{-1}] represents the thermal front velocity. The thermal front velocity becomes (Levec and Carbonell, 1985; Rau et al., 2012),

$$v^t = \frac{\rho_w c_w}{\rho c} q \quad (\text{Eq.2-2})$$

where q is the Darcy velocity of the moving water $\rho_w c_w$ [$\text{Jm}^{-3}\text{C}^{-1}$] is the specific

volumetric heat capacity of water, and ρc [$\text{Jm}^{-3}\text{C}^{-1}$] is the specific heat capacity of the bulk volume of porous media defined as (De Marsily, 1986; Green et al., 1964),

$$\rho c = n\rho_w c_w + (1 - n)\rho_s c_s \quad (\text{Eq.2-3})$$

In the equation above, n is the total porosity of the material and $\rho_s c_s$ [$\text{Jm}^{-3}\text{C}^{-1}$] is the specific volumetric heat capacity of the solids.

The HTE has obvious analogy with solute transport equation (STE). First term of HTE (Eq.1) which represents conduction/dispersion is analogous to diffusion/dispersion term in STE and the second term which represents convection is analogous to the advection term in STE,

$$D^s \nabla^2 C - v^s \cdot \nabla C = \frac{\partial C}{\partial t} \quad (\text{Eq.2-4})$$

where C is the solute concentration, D^s [m^2s^{-1}] represents the solute dispersion coefficient and v^s [ms^{-1}] represents the solute front velocity.

Despite the resemblance between HTE and STE, it is noteworthy that heat propagation in a saturated porous media is fundamentally different from solute transport because it occurs by conduction through both solids and fluid and convection only through the fluid. Since the diffusion and the advection occurs via the fluid alone in the solute transport, there exists a difference between solute and thermal front velocities:

$$v^t = \frac{\rho_w c_w}{\rho c} q = \frac{\rho_w c_w}{\rho c} n_e v^s \quad (\text{Eq.2-5})$$

where n_e is the effective porosity and v^s is defined as $\frac{q}{n_e}$ same as the interstitial or pore velocity.

Under same conditions, the convective transport is slower than solute transport

because the heat capacity of the solids retard the thermal front velocity. On the other hand, conductive heat transport will occur more rapidly than diffusive solute transport (Bear, 1972; De Marsily, 1986). For these reasons, previous studies have suggested that heat transport should be described in a different manner from the way solute transport is described, especially when investigating the thermal dispersion (De Marsily, 1986; Green et al., 1964; Levec and Carbonell, 1985; Lu et al., 2009; Metzger et al. 2004; Rau et al. 2012, 2014).

2.2.2 Thermal dispersion coefficient

The thermal dispersion phenomenon has traditionally been considered analogous to the solute dispersion when applied to natural systems. Accordingly, the thermal dispersion coefficient D^t used in HTE (Eq.1) is generally described as,

$$D^t = \frac{\kappa_0}{\rho c} + \beta \left| \frac{\rho_w c_w}{\rho c} q \right| \quad (\text{Eq.2-6})$$

where κ_0 represents the bulk thermal conductivity which is the geometric mean of the both water and solids conductivities (κ_w and κ_s) and β represents the thermal dispersivity (Rau et al., 2012, 2014). The first part of the equation above is thermal diffusivity and the second part describes thermal dispersion due to convection. Although the linear relationship between the thermal dispersion and the flow velocity have been either accepted or considered insignificantly, a group of authors have revealed a possible non-linear relationship in recent years (De Marsily, 1986; Green et al., 1964; Levec and Carbonell, 1985; Lu et al., 2009; Metzger et al., 2004; Rau et al., 2012; Rau et al., 2014).

Green et al. (1964) conducted the first meaningful laboratory experiment in ideal

porous media with various interstitial velocities between 14.4~180 m/d which they called relatively low fluid velocities. They proposed an empirical relationship for thermal dispersion coefficient in a power law form (Fig. 2-2),

$$\frac{D_l^t}{D_0^t} = n \left(\frac{v^s d_{50}}{D_0^t} \right)^m \quad (\text{Eq.2-7})$$

In the formula above, the subscript l denotes longitudinal direction, d_{50} is the median grain size of porous media and D_0^t is the thermal dispersion at zero flow, that is thermal diffusivity. n and m are empirical coefficients describing the nonlinear increase of thermal dispersion with flow velocity.

Metzger et al. (2004) also experimentally investigated thermal dispersion velocity relationship in ideal porous media, but with higher flow velocities (Darcy velocities up to 812 m/d). Although the range of flow velocity exceeded natural groundwater flow velocities (~130 m/d according to Bear, 1972) and was more close to the forced flow field, power law suggested by Green et al. was still verified in their research.

Lu et al. (2009) performed experiments to reveal the influence of thermal dispersion on heat transport with various water flux (up to 5.2, 4.7 and 3.2 m/d) for three different soil types (sand, silt loam and sandy clay loam). They concluded that the thermal dispersion coefficient is best described by a power law with different coefficients for different soil texture.

Rau et al. (2012) proposed a different empirical formula of thermal dispersion with flow rates in the transition zone where convection begins to dominate conduction in the heat transport mechanism. They considered the transition zone as the range where Darcy velocities are between 22~108 m/d. The formula showed that thermal dispersion coefficient has square relationship with flow velocity (Fig. 2-2).

However, not only does disagreement on the mathematical description of thermal dispersion still exist, but also empirical formulas resulted from previous studies are limited to specific conditions on grain size and flow velocity. Rau et al. (2014) also brought forward the need of further investigation on thermal dispersion in various porous materials to set a better basis for heat tracing.

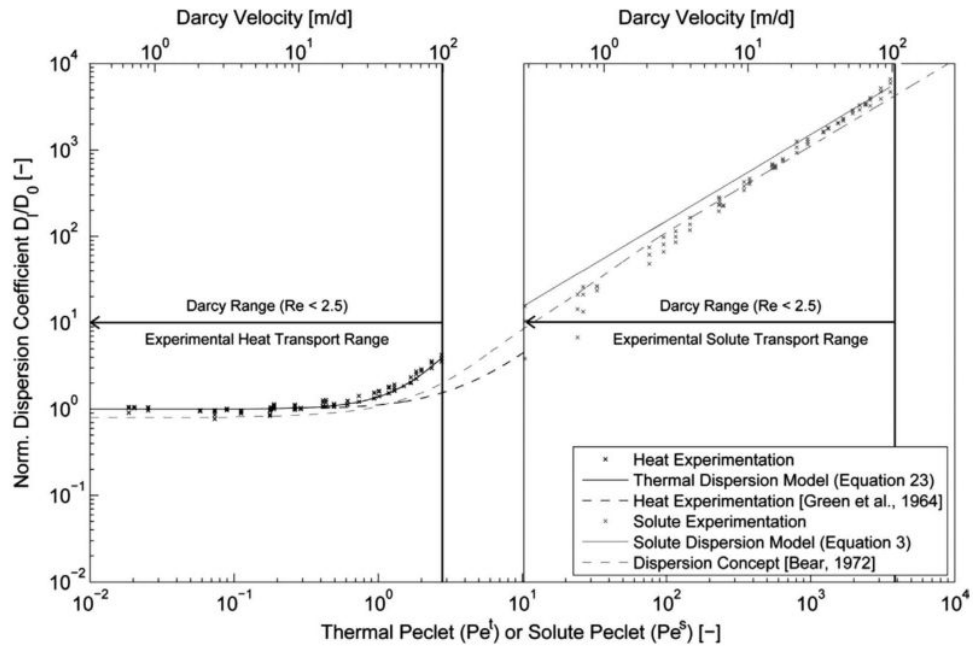


Fig. 2-2. Results of previous researches on the relationship between the thermal dispersion and the flow velocity (Rau et al., 2012).

3 Methods and materials

3.1 Laboratory experiment

3.1.1 Overview of experimental design

The experimental system was designed to investigate the heat transport process in the high flow field caused in GWHP systems. The temperature variation observed from the heat tracer tests with this experimental system was analyzed through comparison with the analytical and the numerical simulation results to estimate the thermal dispersion value and reveal its relationship with flow velocity.

The core of the experimental device consists of a rectangular sand tank made of acryl glass. The size of the sand tank with outer dimension is 1.3 m × 0.6 m × 0.8 m (L × W × D) and the thickness of wall is 1.5 cm. The size was decided after simulating lab-scale experiment through numerical modeling to roughly estimate the thermal plume development. The tank is supported by the manually assembled Aluminum frame surrounding horizontally every 8 cm from the bottom to the top and vertically at four edges (Fig. 3-1a). There are three divided chambers in the tank: a 1 m-length chamber in the middle filled with the sand material and covered by an acryl glass plate with openings, and two chambers of 0.12 m-length each on the both sides used as constant hydraulic head tanks containing different levels of water. These chambers are partitioned by 0.015 m-thick acryl glass plates with a large number of holes so that the water in a higher constant head tank flows through the sand material and creates the uni-directional flow towards the lower head tank. Fine wire mesh (Fig. 3-1c) was attached on the glass plates (on the middle chamber side) to prevent infiltration of sand grains

into the constant head tanks through small holes.

An acrylic pipe of \varnothing 14 mm (inner diameter; i.d.) and 0.7 m in length functions as an injection well. Starting from 0.29m height of the pipe, 0.02m-length portion was drilled to make thin slots so that it can simulate a partially screened well and allow injected water to spread radially from a certain point (Fig. 3-2). The screen section of the well was then wrapped with fine nylon mesh to avoid possible infiltration of sand grains and the clogging issue. As shown in Fig. 3-3 the well pipe is located 0.3 m away from the higher constant head tank on the center line of the middle chamber.

The sand tank is equipped with a measurement system both inside and outside. In addition, there are water inflow/outflow tanks which supply water to the constant head tanks and control the water levels, and a thermostatic water barrel linked to a peristaltic pump for heated water injection (Fig. 3-3). These devices altogether compose the whole laboratory experimental system and the detailed description will be covered later on.

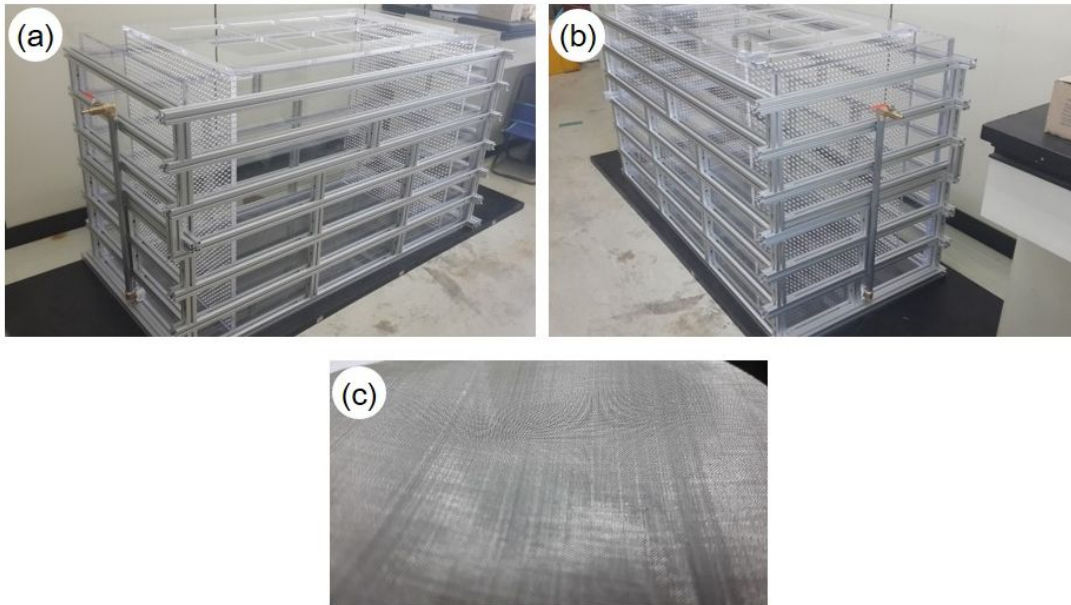


Fig. 3-1. A rectangular acryl glass sand tank (1.3 m x 0.6 m x 0.8 m) supported by manually assembled Aluminum frame (a, b) and fine wire mesh attached on the acryl glass plates between three chambers (c).

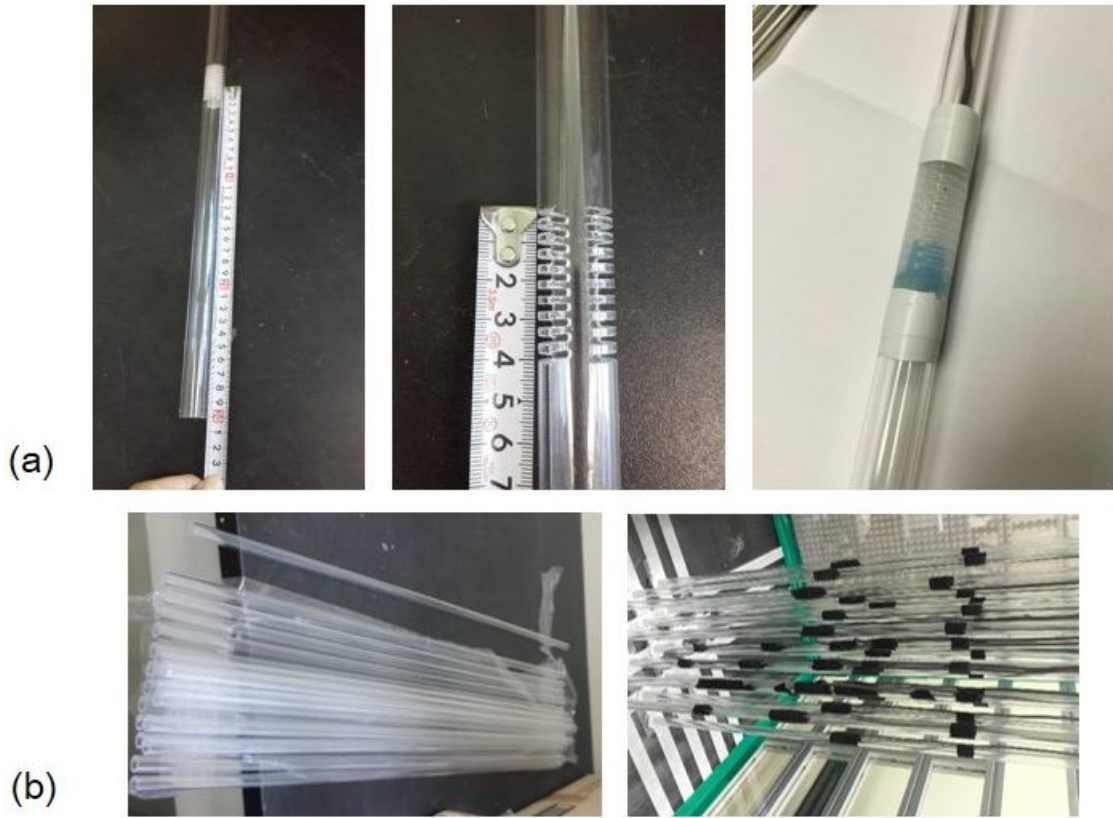


Fig. 3-2. An acrylic pipe of \varnothing 14 mm (i.d.) and 0.7 m length with 0.02 m-wide screen at 0.3 m-height from the bottom (a) and acrylic tubes of \varnothing 8 mm (i.d.) and 0.7 m length used to fix the RTD sensors at the planned locations (b).

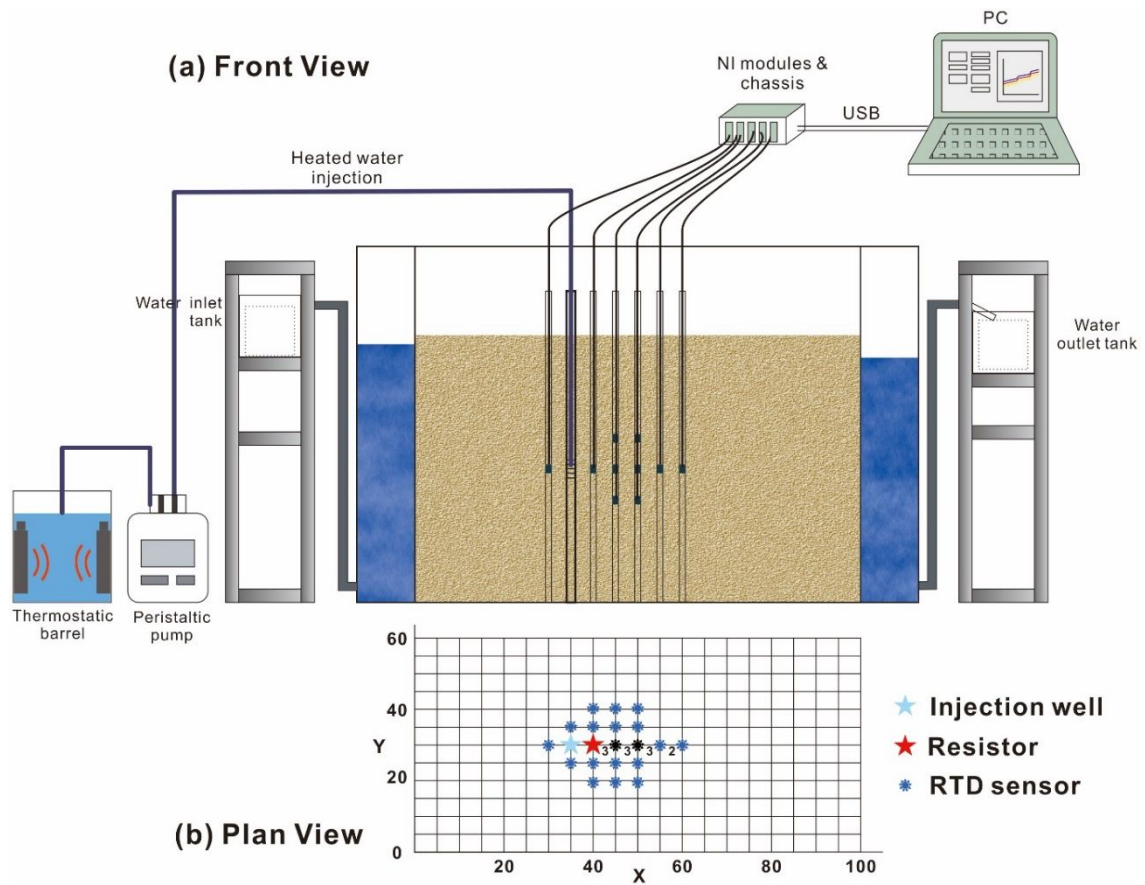


Fig. 3-3. A schematic design of the laboratory experimental system in (a) a front view and (b) a plan view: locations of a resistor (sky-blue star), a well pipe (red star) and RTD sensors (black and blue dots).

3.1.2 Regional flow and well system

As mentioned above, two chambers of the tank which function as constant hydraulic head tanks are connected to water inlet/outlet tanks (Fig. 3-3). Higher head chamber is supplied by the tap water and three drainage tubes mounted at 56.5 cm height on the chamber wall keeps the head constant. Lower head chamber is connected to a water outlet tank placed on an iron stand with adjustable height. By adjusting the height of stand in steps, the elevations of water in lower head chamber are kept below 56.5 cm by up to tens-of-centimeter. The regional water flow caused by the hydraulic head gradient between the two head tanks simulates the uniform natural groundwater flow.

In order to create the forced flow field superposed on the natural groundwater flow field and the thermal plume along the flow, well system was designed. It consists of a thermostatic barrel, a peristaltic pump and PVC tubings (Fig. 3-4). The thermostatic barrel can control and maintain the water temperature up to 40°C even though the difference in temperatures between the regional water and the injected water was set below 5°C to avoid free convection in this experiment. The peristaltic pump extracts and carries the heated water to the well pipe through connected tubings. The end of tubing was located at the 30 cm-height inside the injection well, where the 2 cm-wide screen section allows the injected water to flow throughout the porous medium. Flow rates can be adjusted by changing the tubing size (in diameter) and the RPM of the pump as shown in Fig. 3-5.



(a)



(b)

Fig. 3-4. Well system compositions: (a) a peristaltic pump and PVC tubings (GILSON) and (b) a thermostatic barrel equipped with heaters inside.

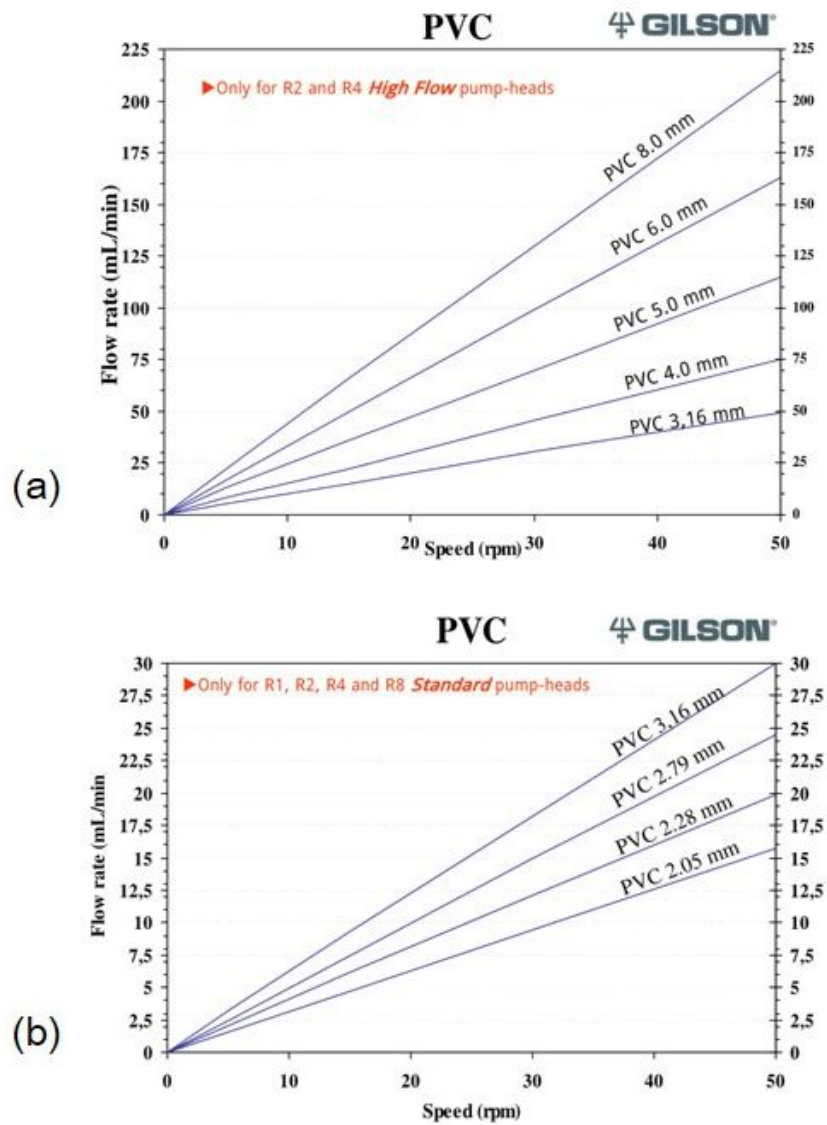


Fig. 3-5. Flow rates chart with different PVC tubing sizes (in diameter) and RPMs of the peristaltic pump with (a) a high flow pump-head and (b) a standard flow pump-head.

3.1.3 Heat sources and sensor equipment

The heat source was given in two types: one is a small resistor that has used in a few previous experiments but with different kind, and the other is warmed water flowing through the slots of injection well that has not been used in a laboratory experiment to estimate the heat dispersion before. A small wire-wound resistor (7 mm in diameter, resistance of 50 Ω , power rating of 5 W) was wrapped with Teflon tape for waterproofing and mounted on the acryl tube at the 30 cm height (Fig. 3-6a). Laboratory DC power supply (AC input: 220V / DC output: 0-30V) applies constant voltage to the resistor with constant current so that the resistor with a constant current flow can act as a continuous heat source (Fig. 3-6b).

A simple performance test of the wire-wound resistor with the established DAQ system was carried out to examine whether the resistor is able to provide constant energy during a certain period of time (Fig. 3-7). Although a laboratory power supply was set to provide constant voltage of 14 V to the wire-wound resistor (50 Ω , 5 W), 0.27 A of constant current flows in the circuit possibly due to the additional resistance from electric cable. The resistor was wrapped with Teflon shrink for waterproofing and immersed in a beaker filled with 200 g of tap water. A RTD sensor was installed right next to the resistor in the center of the beaker to measure temperature change of water and connected to the DAQ hardware and software. LabVIEW system was set to measure the temperature 10 times per second (sampling rate of 10 Hz). A digital stirrer with a small magnetic bar put inside the beaker ensured even heating of water. Fig. 3-8 shows the result of performance test for 33 minutes. After 100 seconds when the resistor started to release heat, the temperature of water increased linearly with time.

For heat tracer tests under forced flow condition, warmed water from the

thermostatic barrel was injected into the injection well and feed through the packed sand. The temperature difference between injected water at the entrance of the pipe and the ambient water was within the range not to cause free convection.

Temperature was measured by resistance temperature detectors (RTD) which ensure better stability and accuracy than thermocouples and thermistors. RTDs are characterized by a linear positive change in resistance with respect to temperature. A thin-film type platinum RTD (Pt100; TSTEC, Korea) was selected in this experiment because of its highly linear response to temperature change and stability as well as its small size (Fig. 3-6c). A RTD element of 2 mm diameter and 2 cm length is connected to extension lead wires in a protective sheath so that it can be supplied with electric current from the device outside the tank. Possible errors due to additional resistance from the lead wires were reduced to negligible levels by using three-wire RTDs. Among the total of 32 RTD sensors, 28 sensors were distributed evenly inside the porous medium while the other sensors are installed outside to measure the temperature of ambient air, water in the thermostat, slotted section of the injection well and the water influent/effluent. One to three RTD sensors were mounted to one acrylic tube of \varnothing 8 mm. Total of 21 tubes with 1 to 3 sensors were arranged around and away from the injection well to make sure that sensors detect thermal plume spreading from the heat source at the exact locations. The array of the tubes and the sensors are shown in Fig. 3-3. The lead wires of RTDs are attached on the tube wall (see Fig. 3-2) and assembled at the top so that the sensors are connected to data acquisition hardware placed outside the tank.

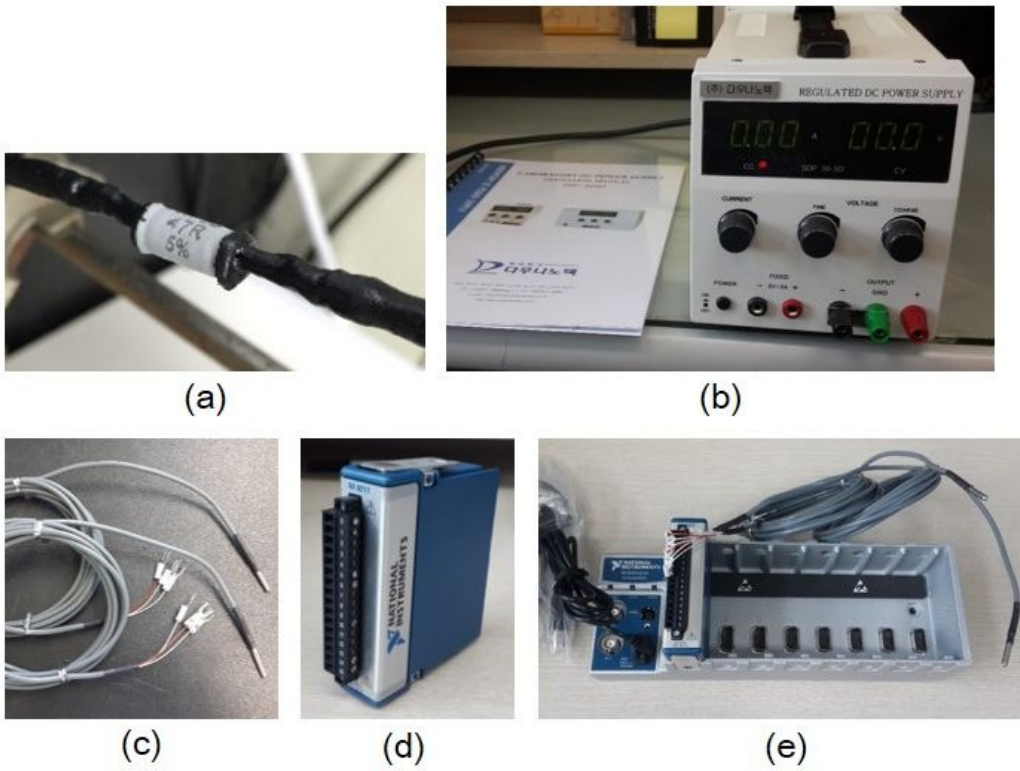


Fig. 3-6. Instruments for heat excitation: (a) a wire-wound resistor and (b) DC power supply, and measurement devices: (c) RTD sensors (Pt 100), (d) NI modules (NI 9217), and (e) eight-slot chassis (NI compact DAQ 9178).

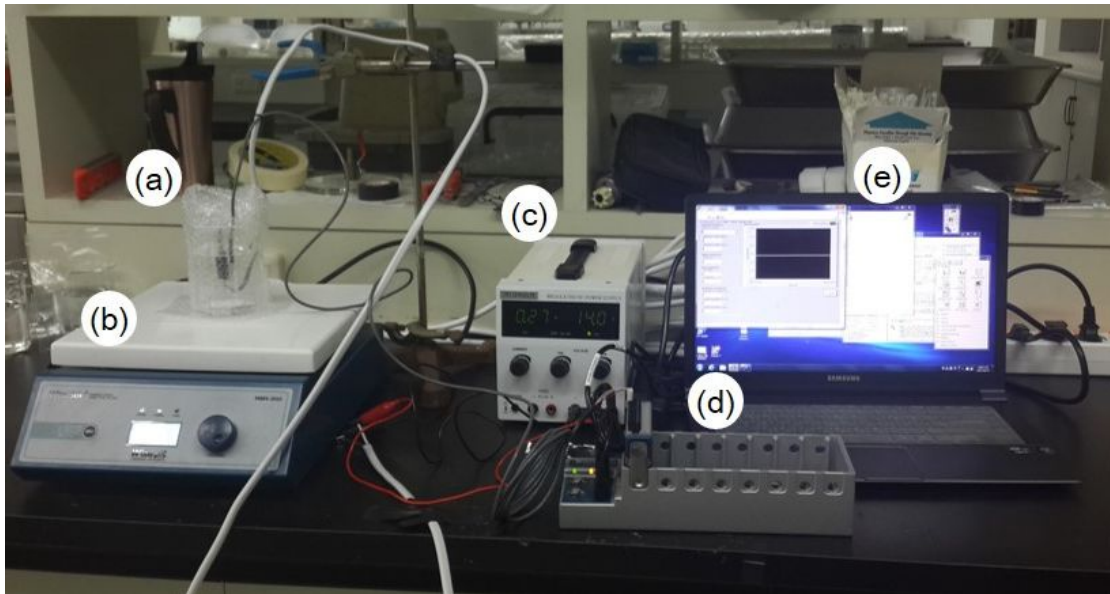


Fig. 3-7. A Setting for the performance test of a wire-wound resistor with the established DAQ system to examine the energy transfer efficiency: (a) an insulated beaker filled with tap water and equipped with a resistor and a RTD sensor, (b) a stirrer, (c) DC power supply, (d) DAQ devices, and (e) the LabVIEW program.

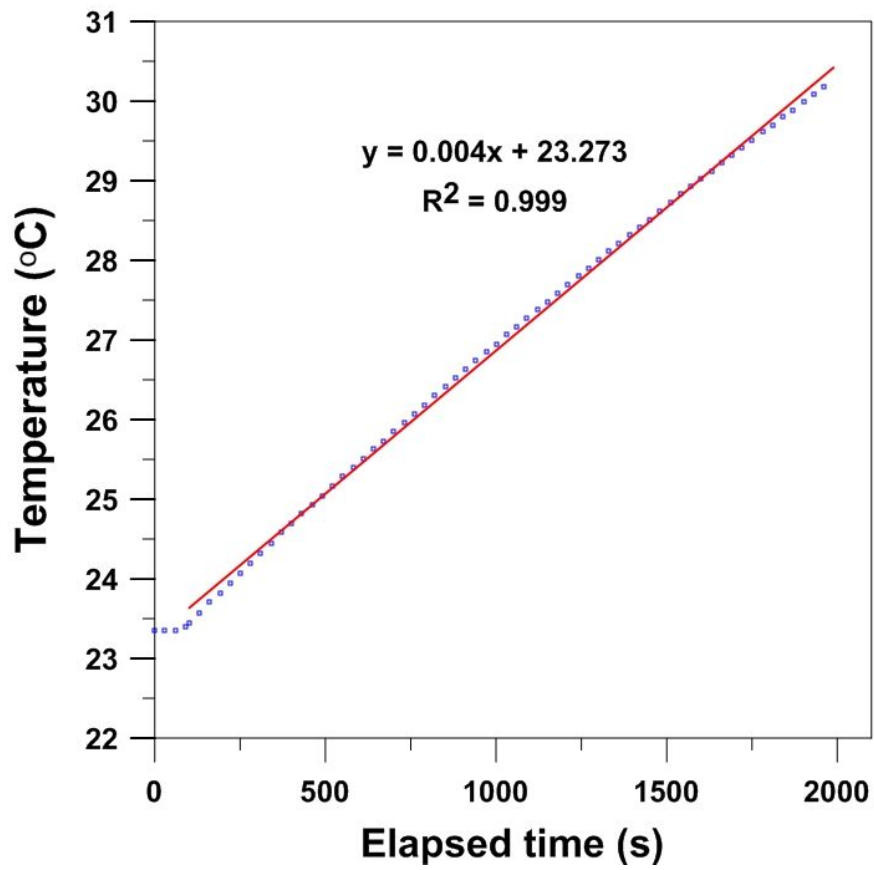


Fig. 3-8. Result of the performance test. Only one data point (blue square) every 30 seconds is shown on the graph and the linear regression curve (red line) indicates constant energy supply from the resistor.

The RTD sensor network was connected to signal conditioning and analog-digital switching modules (NI 9217, National Instruments) mounted on an eight-slot chassis (NI compact DAQ 9178) as shown in Fig. 3-6d and 3-6e. The chassis controls the timing, synchronization and data transfer between modules and an external computer linked to the chassis via USB. These data acquisition hardware (chassis and modules) and software, which consists of a hardware driver and a programming environment, compose a data acquisition (DAQ) system (Fig. 3-9). The hardware driver for the DAQ devices used in the study was NI-DAQmx that provides the interface allowing software to control the devices. Programming environment called LabVIEW 2009 is used to log and visualize the measured data while customizing the data acquisition process such as adjustment of sampling rates.

LabVIEW is a system-design platform and development environment for a graphical programming language which is represented by graphic icons wired on a diagram and then compiled to the machine code that computer processors can run. The programming language used in the LabVIEW is a data-flow programming language, that is, the execution is determined by the structure of graphic icons that users have built. This graphical, and dataflow programming approach allows non-programmers to build programs easily by dragging and dropping visual representations and modify them conveniently. LabVIEW program consists of two windows: (1) the front panel and (2) the block diagram. The front panel, a user interface, is built using controls to supply inputs and indicators to display the outputs. All the objects placed on the front panel appears on the block diagram. The block diagram contains graphical figures of functions that perform operations on controls and supply data to indicators. These controls, indicators, and functions referred to as nodes on the diagram are connected to

one another using wires to complete the program that can be run.

The block diagram designed in this study was modified from an example offered by NI for temperature measuring purpose. It simply consists of virtual channels, task functions and a graphical interface (DAQ assistant) to create, edit and run virtual channels and tasks. Fig. 3-10 shows the compositions and the data flow of block diagram as well as the corresponding controls and indicators on the front panel. Virtual channel function allows users to specify the number of physical channels and input range such as maximum value of temperature. Virtual channels are attached to task functions; timing, start, read, write and save task functions. Timing function controls the timing for hardware-timed data acquisition operations. Start function transitions a task to the running state once start button is clicked on the front panel. Read function is set to read 10 samples per second from each virtual channel and return the data as waveforms. Write function included in DAQ assistant writes samples in signals. Save function on the left generates a memory of written data on the PC.

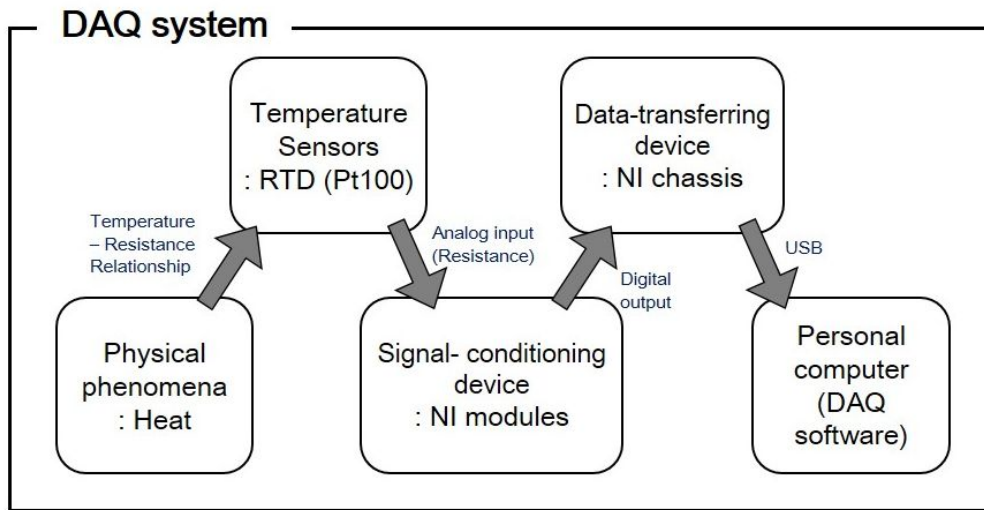
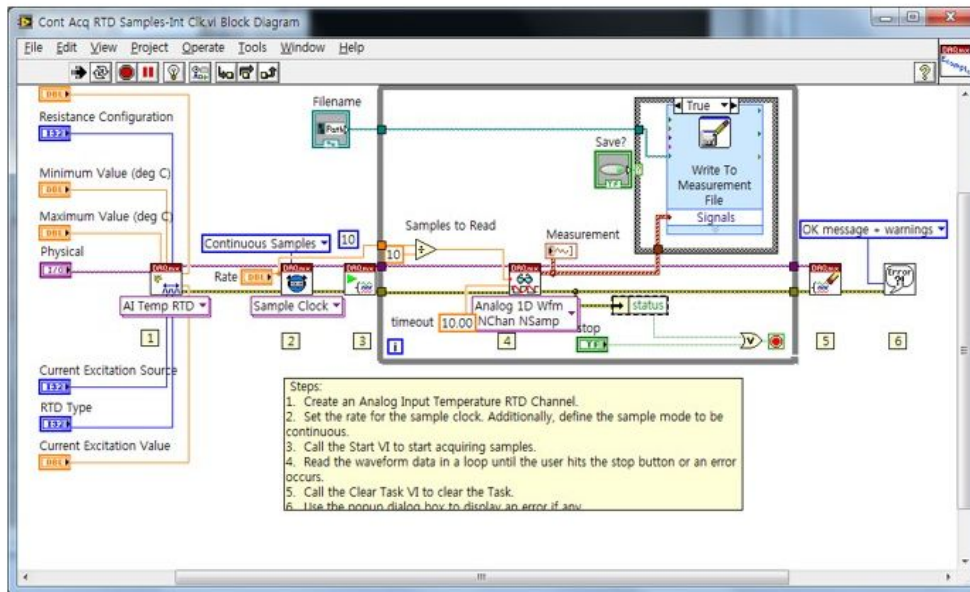
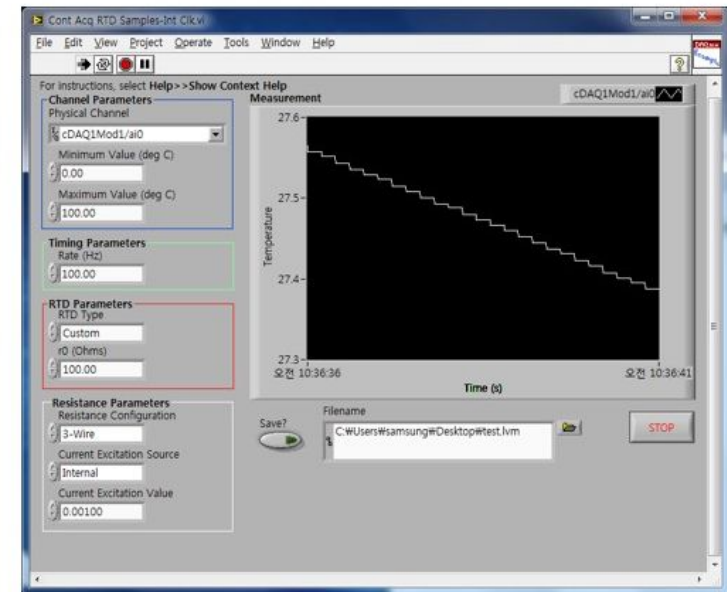


Fig. 3-9. Diagram showing the composition and the mechanism of DAQ (Data Acquisition) system.



(a)



(b)

Fig. 3-10. LabVIEW program designed to acquire temperature data from RTD sensors: (a) the structure of the block diagram and (b) the corresponding objects on the front panel.

3.1.4 Experimental preparation and setup

Before the middle chamber was filled with sand materials (Joomoonjin silica sand), grain size analyses using a set of sieves were performed to identify the median diameter and the uniformity of the porous medium (Fig. 3-11). 15 samples of 200 g dry sand were selected for the sieve analysis to get the representative values for massive dry sand that is planned to be used in the experiment. Six different opening sizes of sieve were used to obtain a smooth cumulative curve by plotting grain size against cumulative weight percent frequency. As shown in Fig. 3-12, by interpolating six grain size – cumulative weight percent points for each sample, 10th, 50th, and 60th percentile diameter (d_{10} , d_{50} , and d_{60}) were estimated. Averaged d_{50} from 15 samples represents grain size of sand material in the tank and uniformity ($U = d_{60}/d_{10}$) indicates the degree of sorting. In general, the medium is considered to be well-sorted if its uniformity is less than 5. The median grain size of sand is 1.28 mm which is within the range of coarse sand but relatively smaller than those used in the previous experiments (Metzger et al., 2004; Rau et al., 2012). The uniformity value showed 1.36 that is considered very well sorted in the study field of sedimentology.

The porosity of the material is decided by measuring the dry sand volume (V_d) and the bulk volume (V_b) according to its mathematical definition,

$$n = \frac{100V_v}{V_b} = \frac{100(V_b - V_d)}{V_b} \quad (\text{Eq.3-1})$$

where V_v is the volume of void space in porous medium. The dry volume of sand samples was observed by carefully dropping 50 ml of water in a 100 ml cylinder half-filled with 50 ml of sand sample and measuring the overall water level rise. Average porosity value from 6 repeated measurement is shown in Table 3-1.

In addition, constant-head permeability tests were performed 6 times repeatedly for 3 samples to estimate hydraulic conductivity of the porous media (Fig. 3-11). Hydraulic conductivity was measured by using a constant-head permeameter where a chamber with an overflow provides water at a constant head while the water flows through the sample at a steady rate and towards another chamber with a lower constant head (Fig. 3-11). The hydraulic conductivity (K) can be obtained by making a slight change to the Darcy's law as follows,

$$Qt = - \frac{KAt(h_A-h_B)}{L} \quad (\text{Eq.3-2})$$

If Qt is replaced with V and h_A-h_B with h, K can be derived from the equation below,

$$K = - \frac{VL}{Ath} \quad (\text{Eq.3-3})$$

where $V[\text{m}^3]$ is the volume of water discharging in time $t[\text{s}]$, $L[\text{m}]$ is the length of the sample, $A[\text{m}^2]$ is the cross-sectional area of the sample, and h is the hydraulic head difference. Three samples of sand that showed maximum, median, minimum d_{50} in the grain size analyses were chosen to estimate the hydraulic conductivity. The test were performed 6 times repeatedly for 3 samples while changing the hydraulic head difference (h). The averaged K value is given in Table 3-1.

Prior to the sand material being packed, the well pipe and thin acryl tubes equipped with sensors were fixed at planned locations with a string to minimize the dislocation of the well and sensors during the setup (Fig.3-13). The resistor and the screen section of injection well were located at 30 cm from the bottom. RTD sensors were distributed around the heat sources horizontally on the X-Y plane (Fig.3-14). Dry sand was carefully packed and then fully saturated with water in several steps to avoid air being

captured inside the porous media (see Fig.3-13). At the height of 45 cm, a soil moisture sensor was buried to measure water contents and to cross-check the porosity. After sand packing had been completed, RTD sensors were connected to DAQ hardware (Fig.3-15). The LabVIEW software was programmed to sample and log temperature 10 times for one second from RTDs. A day after the sand was saturated, water contents was measured by soil moisture sensors buried in the sand to cross-check the porosity value.

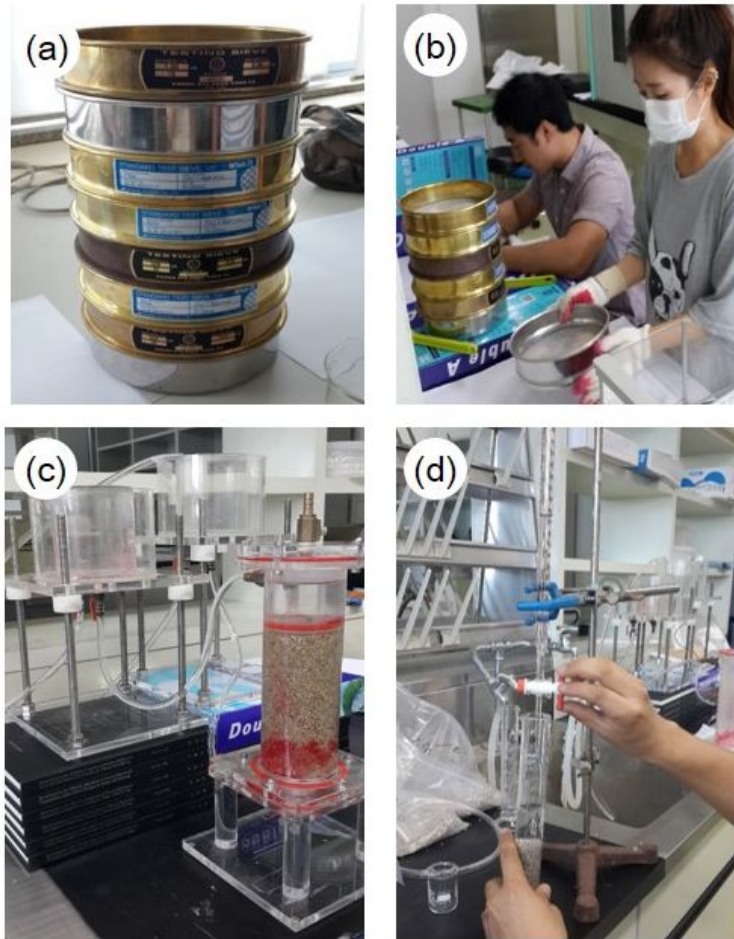


Fig. 3-11. Fundamental analyses to measure physical properties of the sand materials: (a and b) grain size analysis, (c) constant-head permeameter test, and (d) porosity measurement.

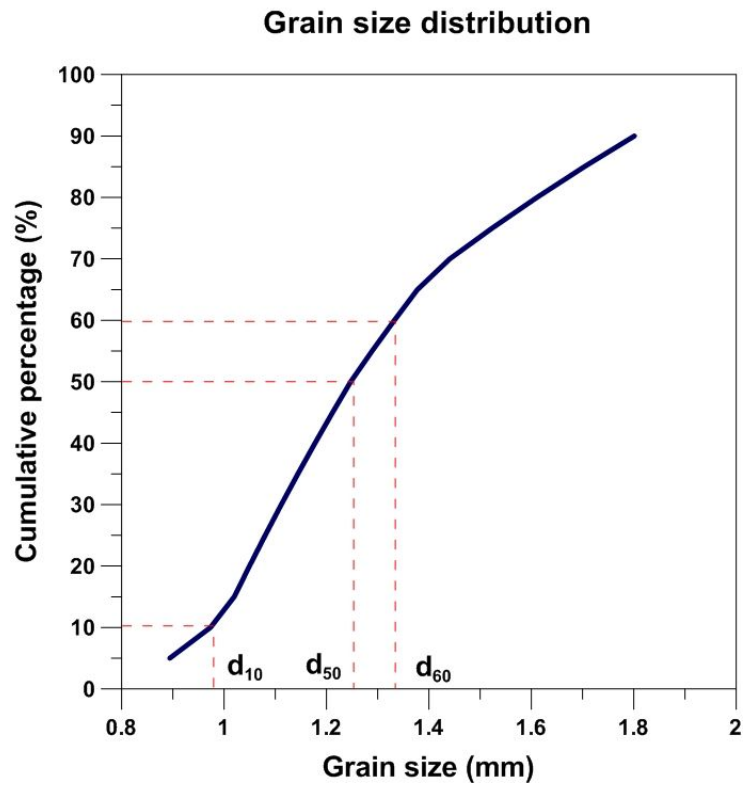


Fig. 3-12. Result of grain size analyses showing the grain size distribution.

Table 3-1. Measured physical properties of porous medium (packed sand)

Properties	d₅₀ (mm)	U (=d₆₀/d₁₀)	K (cm/s)	n
Average	1.28	1.36	0.234	0.34
Standard deviation	0.02	0.01	0.020	0.01

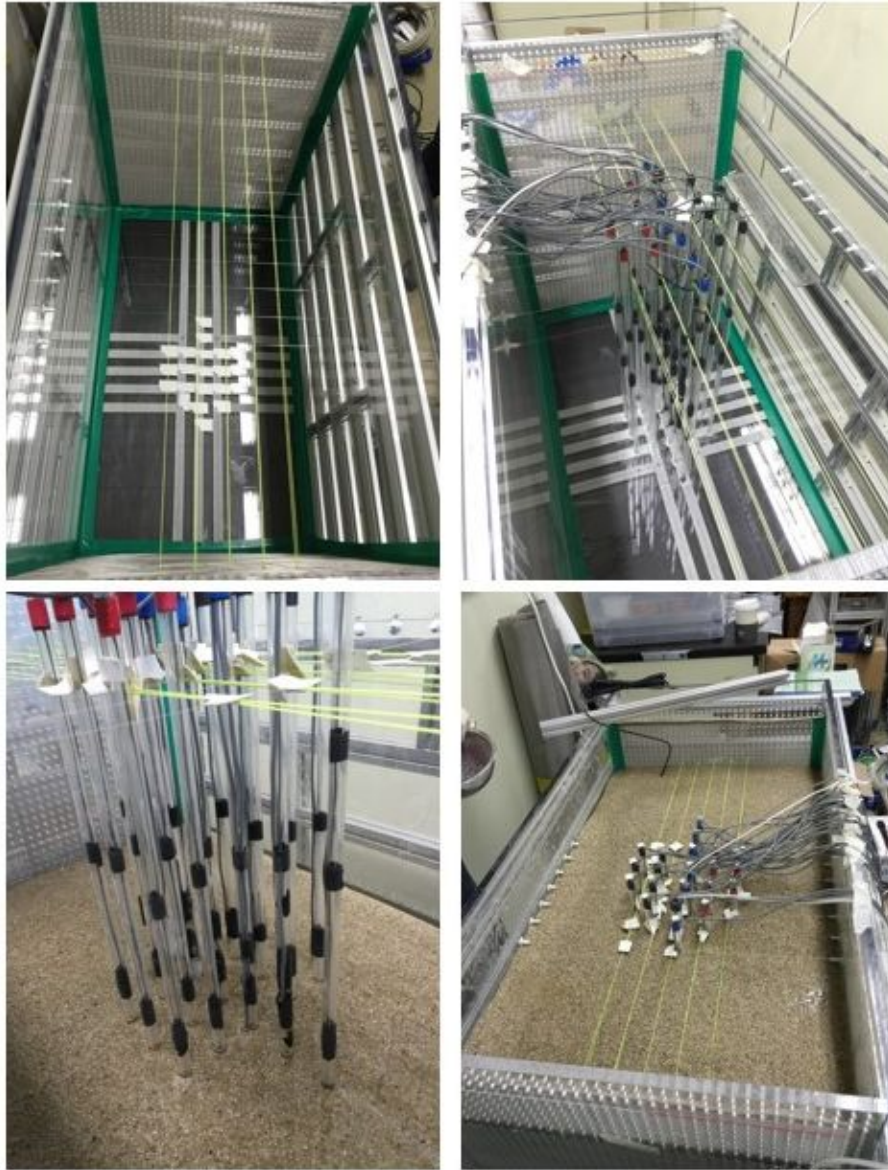


Fig. 3-13. Arrangement of heat sources and sensors (above). Step-wise wet packing of sand materials (below).

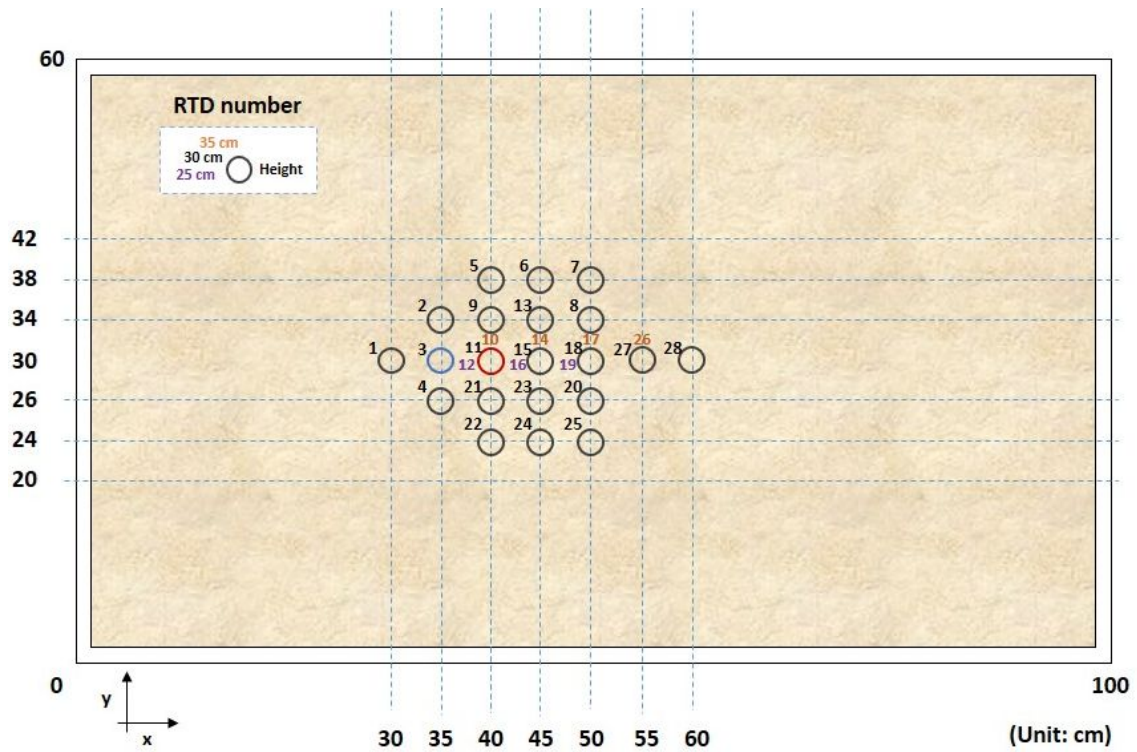


Fig. 3-14. Locations of Heat sources (resistor: red circle, injection point: blue circle) and RTD sensors on the X-Y plane at the height of 0.3 m (z-axis) from the bottom. Actual location of the resistor (0.4, 0.3, 0.3) was considered as a standard point (0, 0, 0) in the analytical approach.



Fig. 3-15. Insulation of experimental device (left) and finishing work of experimental setup with DAQ system connection (right).

3.2 Estimation of thermal dispersion

3.2.1 Analytical approach

In order to interpret the result of heat tracer test without regional flow, an analytical solution (Eq.3-5) for the differential heat transport for heat conduction (Eq.3-4) was fitted with the measurement result.

$$D^t \nabla^2 T = \frac{\partial T}{\partial t} \quad (\text{Eq.3-4})$$

The equation (Eq.3-4) has been solved for an infinite three-dimensional aquitard assuming a quantity of energy Q [W] being injected continuously at the point $(x, y, z = 0)$ by Carslaw and Jaeger (1959). Following is the solution in a modified form (Stauffer et al., 2014).

$$T(x, y, z, t) = T_0 + \frac{Q}{4\pi\kappa_0 r'} \operatorname{erfc}\left(\frac{r'}{\sqrt{4D^t t}}\right) \quad (\text{Eq.3-5})$$

where $r' = \sqrt{x^2 + y^2 + z^2}$ [m], κ_0 is the bulk thermal conductivity [W/m/K], $D^t (= \kappa_0 / \rho c)$ is the bulk thermal diffusivity [m^2/s], Q is the heat flow from the source [W] and erfc means the complementary error function. This analytical solution is also called CPS (Continuous Point Source) model. Thermal conductivity (κ_0) and volumetric heat capacity (ρc) of the porous medium can be derived by fitting the CPS model (Eq.3-5) to the measurement result from the tests without flow. It is important to compute these two thermal properties because they are inserted as input parameters in an analytical model which is used to interpret the results from heat tracer tests with various flow conditions. Also, thermal conductivity of solid fraction (κ_s) and volumetric heat capacity of solid fraction ($\rho_s c_s$) in porous medium can be calculated by Eq.3-6 and Eq.3-7 respectively, which become input parameters in a numerical model.

$$\kappa_0 = \kappa_w^n \cdot \kappa_s^{1-n} \quad (\text{Eq.3-6})$$

$$\rho c = n\rho_w c_w + (1 - n)\rho_s c_s \quad (\text{Eq.3-7})$$

The differential heat transport equation for heat dispersion and convection (Eq.2-1) has been solved for an infinite three-dimensional porous medium with uniform flow in one direction also by Carslaw and Jaeger (1959). The initial condition $T(x, y, z, t = 0) = T_0$ for $-\infty < (x, y, z) < \infty$ and the boundary conditions $Q(0, 0, 0, t > 0) = J$ and $\lim_{x,y,z \rightarrow \pm\infty} Q(x, y, z, t) = 0$ were taken into account where Q (W) is the source strength of a continuous point heat source moving from $(x, y, z = 0)$ in the x-direction. The consequential analytical solution is described in a modified form as,

$$T(x, y, z, t) = T_0 + \frac{Q}{8\pi D_{T,t} \rho c R} \exp\left(\frac{xv^t}{2D_{L,t}}\right) \cdot K(R, t) \quad (\text{Eq.3-8})$$

$$K(R, t) = \left[\exp\left(-\frac{Rv^t}{2D_{L,t}}\right) \operatorname{erfc}\left(\frac{R-v^t}{2\sqrt{D_{L,t}t}}\right) + \exp\left(\frac{Rv^t}{2D_{L,t}}\right) \operatorname{erfc}\left(\frac{R+v^t}{2\sqrt{D_{L,t}t}}\right) \right] \quad (\text{Eq.3-9})$$

$$R = \sqrt{x^2 + \frac{D_{L,t}}{D_{T,t}}(y^2 + z^2)} \quad (\text{Eq.3-10})$$

where $D_{L,t}$ and $D_{T,t}$ are the longitudinal thermal dispersion coefficient assumed to occur in the x direction and the transverse thermal dispersion coefficient assumed to occur on a plane at right angles, respectively (Carslaw and Jaeger, 1959; Rau et al., 2012). This analytical solution is also called MCPS (Moving Continuous Point Source) model. By fitting the MCPS model result (Eq.3-8) to the temperature response from heat tracer tests under various flow conditions, longitudinal/transverse thermal dispersion coefficient and the thermal front velocity can be estimated.

3.2.2 Numerical approach

A numerical model was used to compute temperature distribution around the water injection point in the porous medium under various flow conditions and estimate the thermal dispersion coefficient. In this study, FEFLOW, which is based upon finite element code (FEM) and can deal with solute and heat transport as well as groundwater flow in porous media was used to estimate the heat tracer movement in the sand tank. The numerical code is basically governed by the conservation laws for mass, momentum, and energy for solid, liquid and gas phases as follows (Diersch, 2005),

(1) Mass conservation of α phase

$$\frac{\partial}{\partial t}(\varepsilon_{\alpha}\rho^{\alpha}) + \frac{\partial}{\partial x_i}(\varepsilon_{\alpha}\rho^{\alpha}v_i^{\alpha}) = \varepsilon_{\alpha}\rho^{\alpha}Q_{\rho}^{\alpha} \quad (\text{Eq.3-11})$$

(2) Momentum conservation of α phase

$$v_i^{\alpha} + \frac{k_{ij}^{\alpha}}{\varepsilon_{\alpha}\mu^{\alpha}}\left(\frac{\partial p^{\alpha}}{\partial x_i} - \rho^{\alpha}g_j\right) = 0 \quad (\text{Eq.3-12})$$

(3) Energy conservation of α phase

$$\frac{\partial}{\partial t}(\varepsilon_{\alpha}\rho^{\alpha}E^{\alpha}) + \frac{\partial}{\partial x_i}(\varepsilon_{\alpha}\rho^{\alpha}v_i^{\alpha}E^{\alpha}) + \frac{\partial}{\partial x_i}(j_{iT}^{\alpha}) = \varepsilon_{\alpha}\rho^{\alpha}Q_T^{\alpha} \quad (\text{Eq.3-13})$$

where α is the phase indicator, ε_{α} is the volume fraction of phase α ($\sum \varepsilon_{\alpha} = 1$); ρ^{α} is the density of α phase [kg/m^3]; v_i^{α} is the velocity vector of α phase [m/s]; Q_{ρ}^{α} and Q_T^{α} are the mass and heat supply of α phase, respectively; k_{ij}^{α} is the permeability tensor of α phase [m^2]; μ^{α} is the viscosity of α phase [$\text{kg}/\text{m}\cdot\text{s}$]; p^{α} is the pressure of α phase; g_j is the gravity vector; E^{α} is the internal (thermal) energy of α phase; and j_{iT}^{α} is the Fourierian heat flux vector of α phase.

A preliminary 2-D modeling was performed by using FEFLOW to predict the

extent of thermal plume from the heat source and the adequate running time before the actual test. A finite element grid was constructed for a 2-D model domain with dimensions of 1.0 m x 1.0 m (Fig. 3-16). The model domain, which has one point heat source and six observation points, was discretized into square elements ($\Delta x = \Delta y = 0.01$ m). Simulations were performed under steady water flow and transient transport conditions. The initial time step was set to be 10^{-5} d with a maximum time step of 10^{-3} d. The model input parameters are listed in Table 3-2. As shown in Fig. 3-16, Neumann boundary condition was assigned at the specific node to represent the point heat source of 5 W. The numerical simulations were run for maximum 6 hours under various groundwater flow velocities. Fig. 3-17 shows the results of 2-D heat transport simulations. As the groundwater flow velocity increases, the transverse extent of thermal plume decreases and remains within 0.3 m from the heat source during the simulation. Under no flow condition, however, thermal plume was predicted to extend over 0.3 m from the source. With reduced simulation time of 3hrs, the results showed that the transvers extent stayed within 0.3 m from the source even under no flow condition. Based upon these results, the tests were planned to be run for up to 3 hours.

Numerical simulations for the actual heat tracer test with water injection were performed first to validate the numerical model by fitting the simulation results with the experimental results. Then, further numerical simulations were conducted to fairly compare the thermal dispersion behavior in the forced flow condition caused by warm water injection with that in the natural flow condition where the same amount of heat is supplied by a resistor. The 3-D model domain with the dimensions of 1.0 m x 0.6 m x 0.6 m (L x W x D) was discretized after the grid convergence test. To grasp the temperature responses around an injection point and observation points better, the grid

was selectively designed: (i) from $x = 0.3$ m, $y = 0.26$ m to $x = 0.6$ m, $y = 0.34$ m, the square elements were sized $\Delta x = \Delta y = 0.002$ m and (ii) $\Delta x = \Delta y = 0.004$ m throughout the rest (Fig.3-18). The initial time step was set to be 10^{-9} d with a maximum time step of 10^{-4} d (Fig.3-19). Fig.3-20 shows the location of heat source and observation points and boundary conditions applied in the numerical simulations. Initial water level was assumed to be zero all over the domain. To consider the groundwater flow, hydraulic gradient was set from 0.0 to 0.15 on the left and right sides of the model domain as Dirichlet boundary condition. Initial temperature of the subsurface was different depending on the actual test condition when validating the model. Then, time-variant Dirichlet boundary condition was inserted at the injection point to represent the injection of warm water with some variation in its temperature. On the other hand, when performing further case simulations, initial temperature was fixed at 14 °C for all the cases. At the injection point, constant Dirichlet boundary condition was applied simulating consistent heat flow resulted from water injection. The model input parameters are listed in Table 3-3.

Table 3-2. Hydrogeological and thermal parameters used for 2-D model simulation

Parameter	Symbol	Unit	Value
Transmissivity	T	10^{-4} m ² /s	0.6
Anisotropy factor	α	-	1
Specific storage	S _s	10^{-4} m ⁻¹	1
Aquifer thickness	b	m	0.6
Porosity	n	-	0.3
Volumetric heat capacity of solid	$\rho_s c_s$	10^6 J/m ³ -K	2.52
Volumetric heat capacity of fluid	$\rho_w c_w$	10^6 J/m ³ -K	4.2
Thermal conductivity of solid	κ_s	W/m-K	3
Thermal conductivity of fluid	κ_f	W/m-K	0.65
Longitudinal thermal dispersivity	β_L	m	5
Transverse thermal dispersivity	β_T	m	0.5

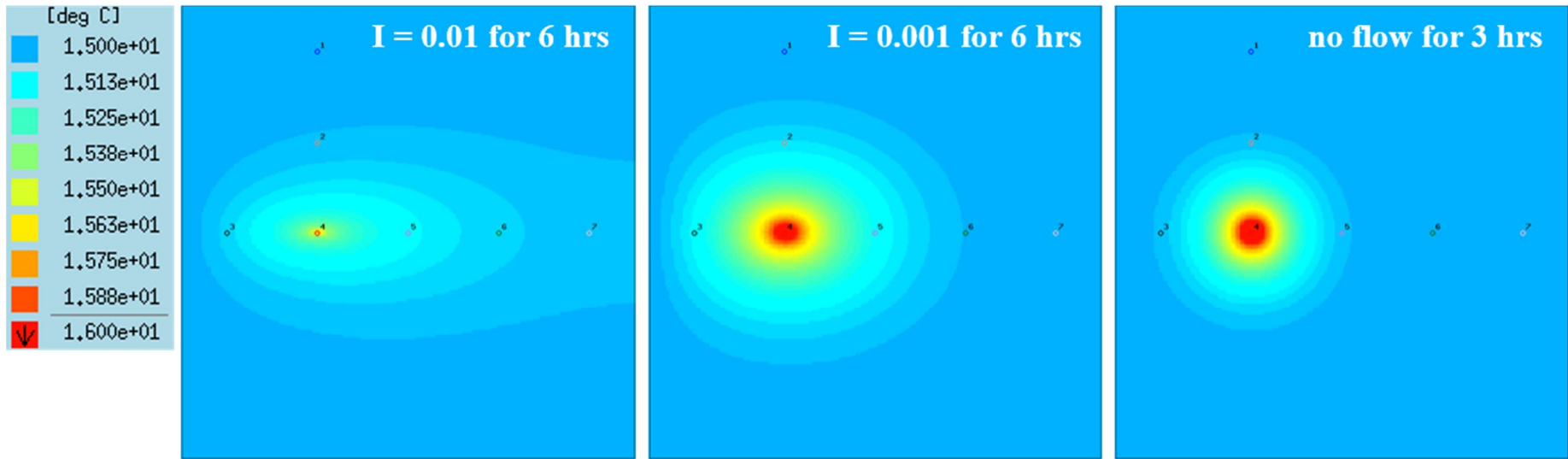


Fig. 3-17. Results of preliminary 2-D heat transport simulations using FEFLOW under different flow velocities.

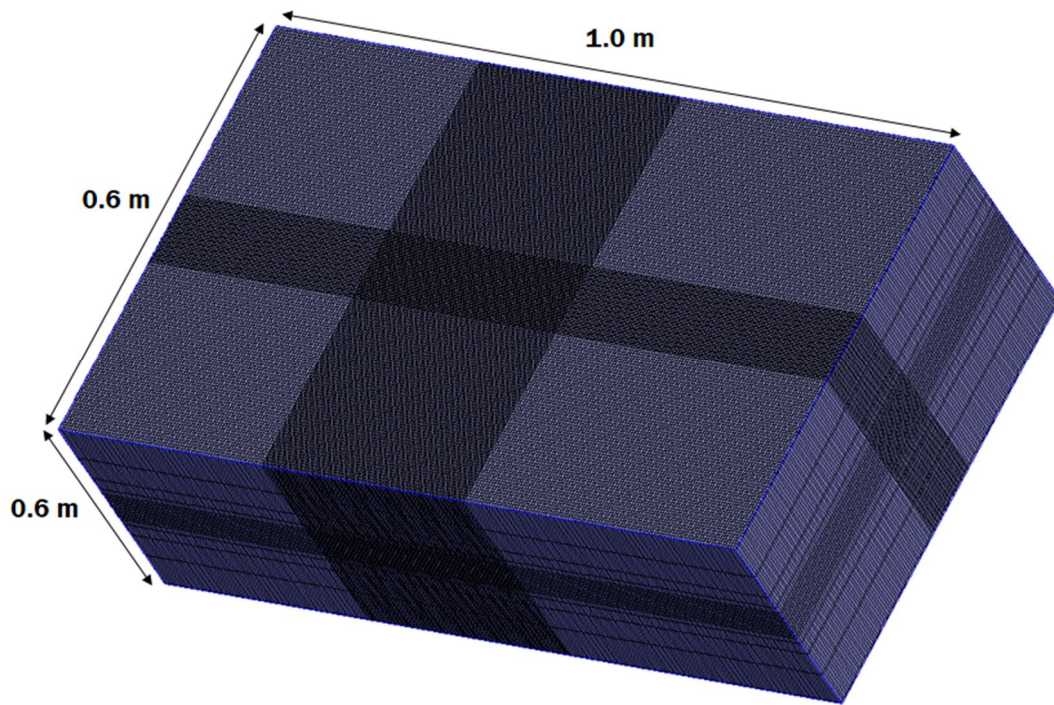


Fig. 3-18. Spatial discretization of the 3-D model domain.

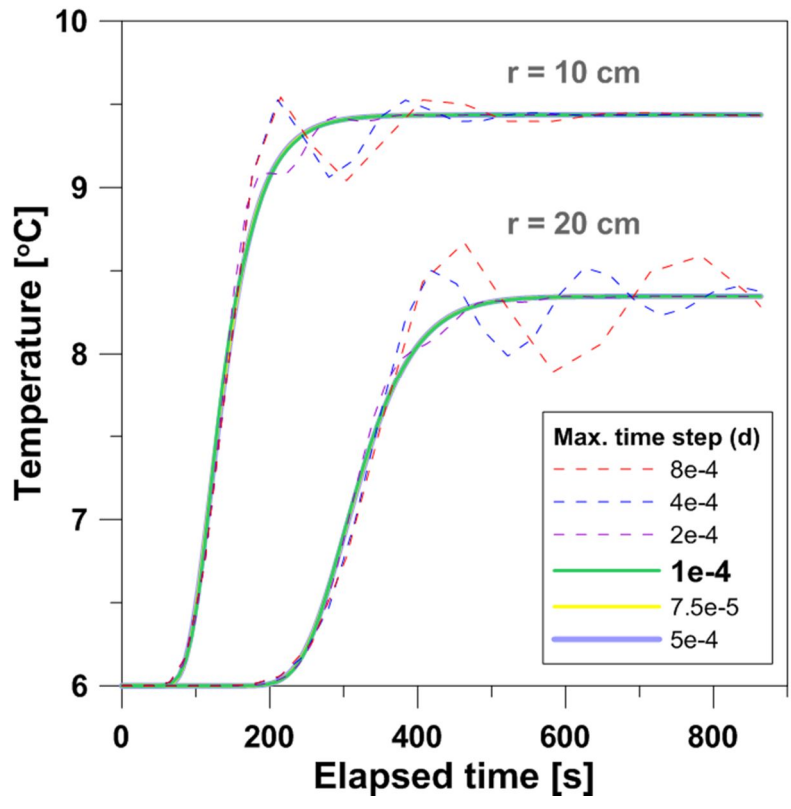


Fig. 3-19. Determination of temporal discretization in 3-D heat transport simulation.

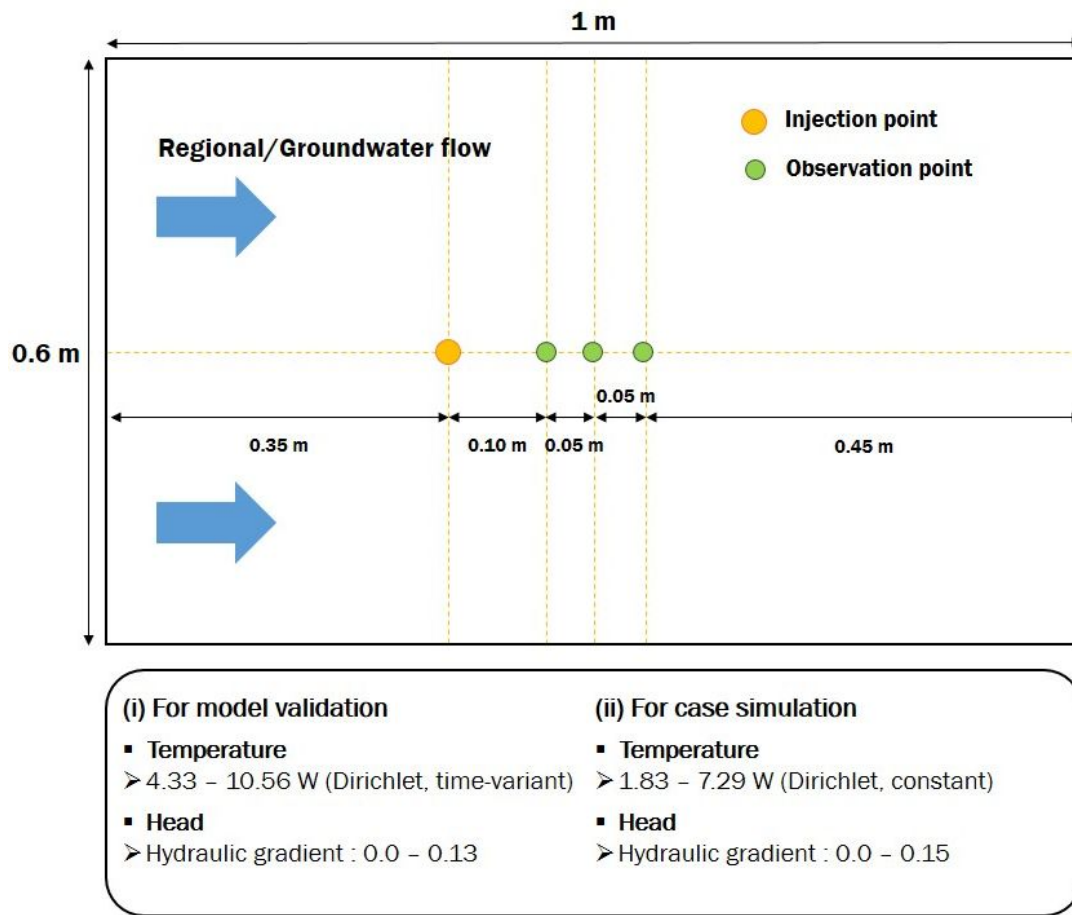


Fig. 3-20. Schematic model domain (in x-y plan view) and boundary conditions for 3-D heat transport simulation.

Table 3-3. Hydrogeological and thermal parameters used for 3-D model simulation

Parameters	Symbol	Unit	Temperature*	Value
Transmissivity	T	$10^{-3} \text{ m}^2/\text{s}$		1.4
Anisotropy factor	α	-		1.0
Specific storage	S_s	10^{-4} m^{-1}		1.0
Aquifer thickness	b	m		0.6
Porosity	n	-		0.331
Volumetric heat capacity of water**	$\rho_w c_w$	$10^6 \text{ J/m}^3\text{-K}$	6 °C	4.202
			12 °C	4.187
			14 °C	4.175
Thermal conductivity of water**	κ_w	W/m-K	6 °C	0.572
			12 °C	0.584
			14 °C	0.587

*Thermal properties of water depending on the temperature condition of the experiment

**Reference: NIST (National Institute of Standards and Technology) www.nist.gov/

3.2.3 Parameter estimation

Thermal parameters and flow velocity were estimated by matching temperature time series data measured by the DAQ system with the data computed from the analytical model or the numerical model (FEFLOW) depending on the heat source type. In the heat tracer test using a wire-wound resistor as a point heat source, temperature time series data at several locations was fitted to the temperature breakthrough curve obtained from the analytical solutions (Eq.3-5 and 3-8). By performing heat tracer tests under no-flow condition and analyzing the result first, the location of the sensors was corrected and thermal parameters (κ_0 and ρc) were estimated. The reason correction of RTD sensors' location is necessary is that wet-packing of sand material might have caused a slight dislocation, although the sensors were installed as planned in designing process. These estimated parameters were then used to interpret all the subsequent convective/dispersive heat transport experiments. Temperature response data from heat tracer tests under different flow conditions was fitted to the data computed from the analytical model (Eq.3-8) On the other hand, measured temperature data from the heat tracer tests with injection of warmed water was matched with the result of the numerical model which simulated the heat transport under the forced groundwater flow condition.

It is important in numerical modeling to determine dimensions of the model domain and discretize space and time reasonably as well as to set the initial and boundary conditions to reflect the real experiment conditions. It is also crucial for both analytical and numerical models that model input parameter should have the values within reasonable ranges. The quality of fit between the observation and the model results was evaluated by the root mean square error (RMSE):

$$\text{RMSE} = \left[\sum_{i=1}^n \frac{(M_i - S_i)^2}{n} \right]^{1/2} \quad (\text{Eq.3-14})$$

where M_i is the measured value and S_i is the simulated value. When RMSE is minimized, the parameters of interests (especially, the thermal dispersion coefficient) can be estimated from the best fit. In a curve fitting process for heat tracer tests with and without regional flow, three parameters of interests were derived respectively. The least RMSE and the corresponding parameters were calculated by using MATLAB code.

4 Results and discussions

4.1 Heat tracer tests using a resistor without regional groundwater flow

Lab-scale heat tracer test using a resistor with no-flow condition was performed first in order to estimate thermal properties of the porous medium by matching the test result with one from the analytical model (CPS model) for conductive heat transport process (Eq.3-5). Before the test was conducted, a few hours of temperature stabilization throughout the porous medium had been proceeded. Once the temperature became steady, constant power of 4.712 W was supplied via the electric wire linked to the resistor inside porous medium. Because there was no regional water flow, heat from the resistor was transferred only by conduction between solids and water. Fig.4-1 shows the concept of heat transport process under no regional flow in this experiment. Temperature response at every location where RTD sensor is installed was monitored in real-time through the front panel window of LabVIEW software and logged at a sampling rate of 0.1 s. The whole running time of the experiment did not exceed 3 hours considering that thermal plume nearly approached the wall after 3 hours in the preliminary modeling. The same experiment was repeated one more time afterwards. Fig.4-2 and 4-3 displays the temperature breakthrough curves obtained by the measurement (in cross-shape symbol) and the CPS model results (in a solid line). As mentioned before, the best fit between the measured data and the model was found by the MATLAB code specially generated to derive parameters of interest when RMSE is the least. Table 4-1 shows the corrected (x, y) locations, thermal conductivity, and volumetric heat capacity values at several RTDs around the heat source. Even though so

much effort was put when fixing sensors at the predetermined locations during experimental setup, there was a slight dislocation. Thermal conductivity and volumetric heat capacity values of solid that were averaged from two repeated tests. On average, volumetric heat capacity value of the solid fraction of porous medium ($\rho_s c_s$) was $1.88 \times 10^6 \text{ J/m}^3/\text{K}$ which is within an acceptable range compared to the references provided below Table 4-1. However, the reason thermal conductivity value (κ_s) of 3.32 W/m/K (on average) in this experiment seem to stray from the reference range for dry sand is that the value can highly differ depending on the Quartz ($\kappa = 7.2 \sim 8.4 \text{ W/m/K}$) contents. Thermal conductivity of solid in soil can be calculated as $\kappa_{solid} = \kappa_{quartz}^{V_{quartz,s}} \kappa_{min}^{1-V_{quartz,s}}$ where $V_{quartz,s}$ is the volumetric proportion of quartz in soil solids, and κ_{quartz} and κ_{min} mean thermal conductivity of quartz and non-quartz minerals, respectively (Balland and Arp, 2005). The least RMSE and NRMSE (Normalized RMSE) which is RMSE divided by total the temperature increase are also reported in Table 4-1.

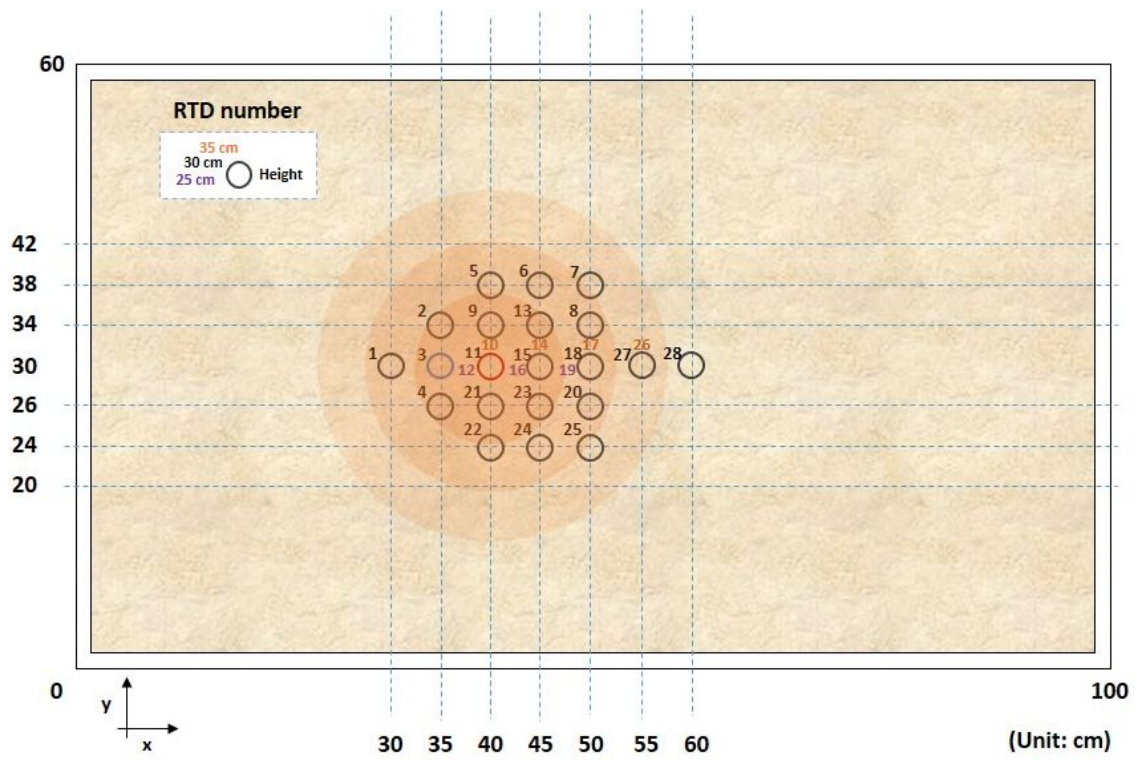


Fig. 4-1. Concept of the heat tracer test without regional flow and the heat transfer process only related to heat conduction (thermal plume described as orange concentric circles).

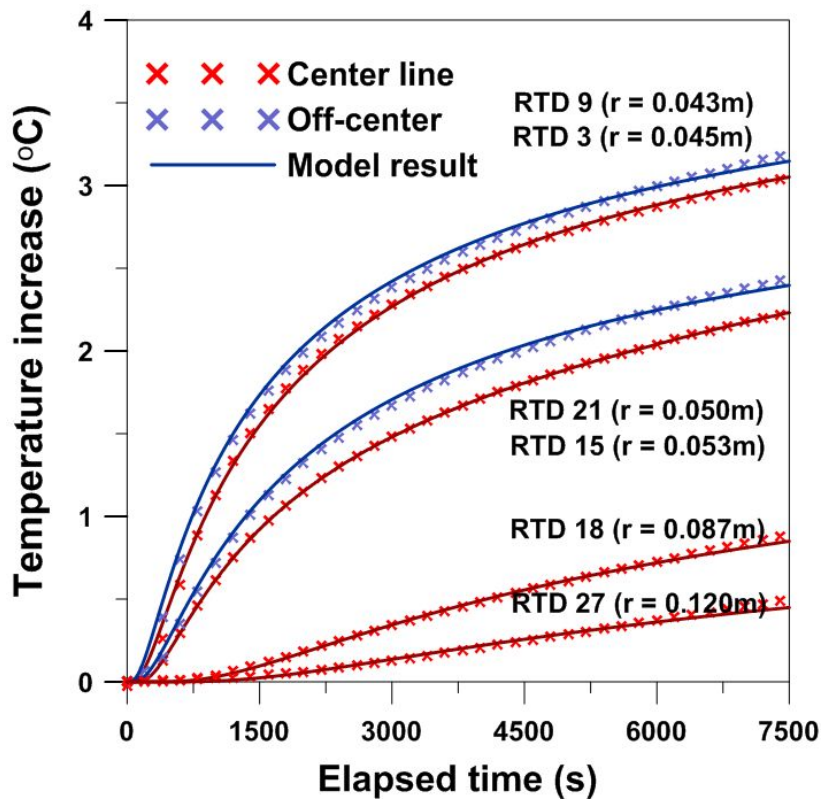


Fig. 4-2. The temperature breakthrough curves obtained by the measurement (in cross-shape symbol) and the CPS model results (in a solid line) for the first experiment. RTDs on the center line (in a red color) is located along the x-axis away from the heat source. The distance (r) from the heat source was computed when the best fit was met.

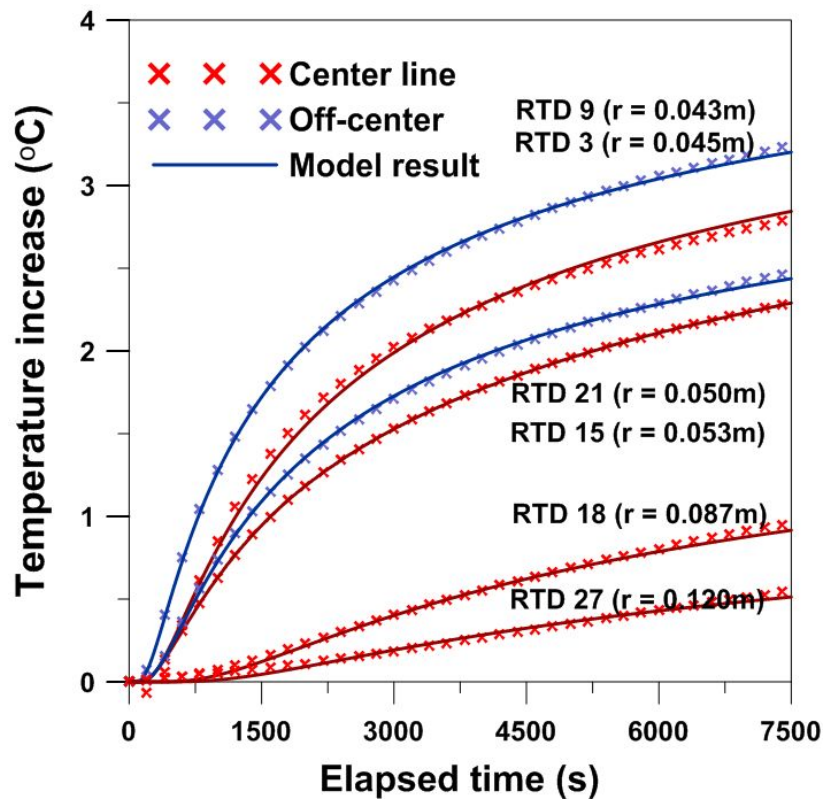


Fig. 4-3. The temperature breakthrough curves obtained by the measurement (in cross-shape symbol) and the CPS model results (in a solid line) for the repeated experiment.

Table 4-1. Thermal properties of porous medium and sensor location derived from the best fit between measurements and the model

Parameters	RTD 3	RTD 8	RTD 9	RTD 13	RTD 15	RTD 18	RTD 21	RTD 23	RTD 27
x [m]	-0.045	0.082	0	0.050	0.053	0.087	0	0.054	0.120
y [m]	0	0.036	0.043	0.036	0	0	-0.050	-0.047	0
z [m]	0	0	0	0	0	0	0	0	0
$\rho_s c_s$ [J/m ³ /K]*	1,693,897	1,989,724	1,689,984	2,296,977	1,906,402	2,238,507	1,945,011	1,656,263	1,508,339
κ_s [W/m/K]**	3.164	2.974	3.444	3.482	3.555	3.114	3.544	3.086	3.516
RMSE	0.025	0.012	0.017	0.015	0.020	0.012	0.015	0.013	0.017
NRMSE	0.009	0.014	0.005	0.009	0.009	0.013	0.006	0.009	0.033

* Reference range for volumetric heat capacity of dry sand / quartz(mineral) : $1.3 - 1.6 \times 10^6$ J/m³/K (Stauffer et al., 2014) / 2.01×10^6 J/m³/K (Balland and Arp, 2005)

** Reference range for thermal conductivity of dry sand / quartz(mineral) : $0.3 - 0.8$ W/m/K (Stauffer et al., 2014) / $7.2 - 8.4$ W/m/K (Balland and Arp, 2005)

4.2 Heat tracer tests using a resistor under various flow conditions

Lab-scale heat tracer tests using a resistor under a variety of flow condition were performed to estimate thermal dispersion coefficient of porous medium by matching the test result with one from the analytical model (MCPS model) for convective heat transport (Eq.3-8). The same amount of constant electric power was fed to the resistor, the heat source. 10 different regional flow velocities up to 36 m/d were applied in each heat tracer test to examine the relationship of thermal dispersion coefficient with Darcy velocity (q) (or thermal front velocity, v^t) suggested by previous studies. Fig.4-4 shows the concept of heat transport process with regional flow being fed through the sand tank. Before each heat tracer test was conducted, a few hours of temperature stabilization throughout the porous medium and hydraulic gradient adjustment afterwards had been proceeded. Hydraulic gradient was changed by controlling the elevation of lower constant-head tank. Each experimental running time was shorter than the test without flow because the heat from the resistor transferred by dispersion and convection in this case. As regional flow velocity increased, the time for temperature response at sensors to reach the steady-state became shorter.

Fig.4-5 through Fig.4-9 show the temperature breakthrough curves obtained by the measurement (in cross-shape symbol), especially the RTD sensors on the center-line and the MCPS model results (in a solid line). Derived thermal properties and the corrected sensor locations from no-flow test were applied in MCPS model (Eq.3-8) as fixed variables so that parameters of interests in this experiment can be derived with better reliability. The MCPS model results with the least RMSE and the corresponding thermal dispersion coefficients and thermal front velocity were computed from the MATLAB code mentioned above. In Table 4-2, estimated longitudinal/transverse thermal

dispersion coefficients ($D_{L,t}/D_{T,t}$) and thermal front velocity (v^t) are recorded for each flow condition in the heat tracer test. Derived $D_{L,t}$ ranged from 6.0×10^{-7} to 1.4×10^{-6} m^2/s and $D_{T,t}$ from 8.3×10^{-7} to 1.6×10^{-6} m^2/s . Thermal dispersion coefficients, especially $D_{L,t}$, showed increasing trend with thermal front velocity (v^t). Regression analysis of the parameters resulted in a linear increasing trend between longitudinal thermal dispersion coefficient ($D_{L,t}$) and thermal front velocity (v^t) with $R^2 = 0.718$. However, the result of regression analysis indicated that $D_{L,t}$ values can also be described by non-linear increasing trend with v^t with $R^2 = 0.621$ (Fig.4-10). Further discussion on the description of longitudinal thermal dispersion coefficient ($D_{L,t}$) will be covered later on. For the transverse thermal dispersion coefficient ($D_{T,t}$), its linear increasing trend with thermal front velocity (v^t) showed lower $R^2 = 0.493$ (Fig. 4-11).

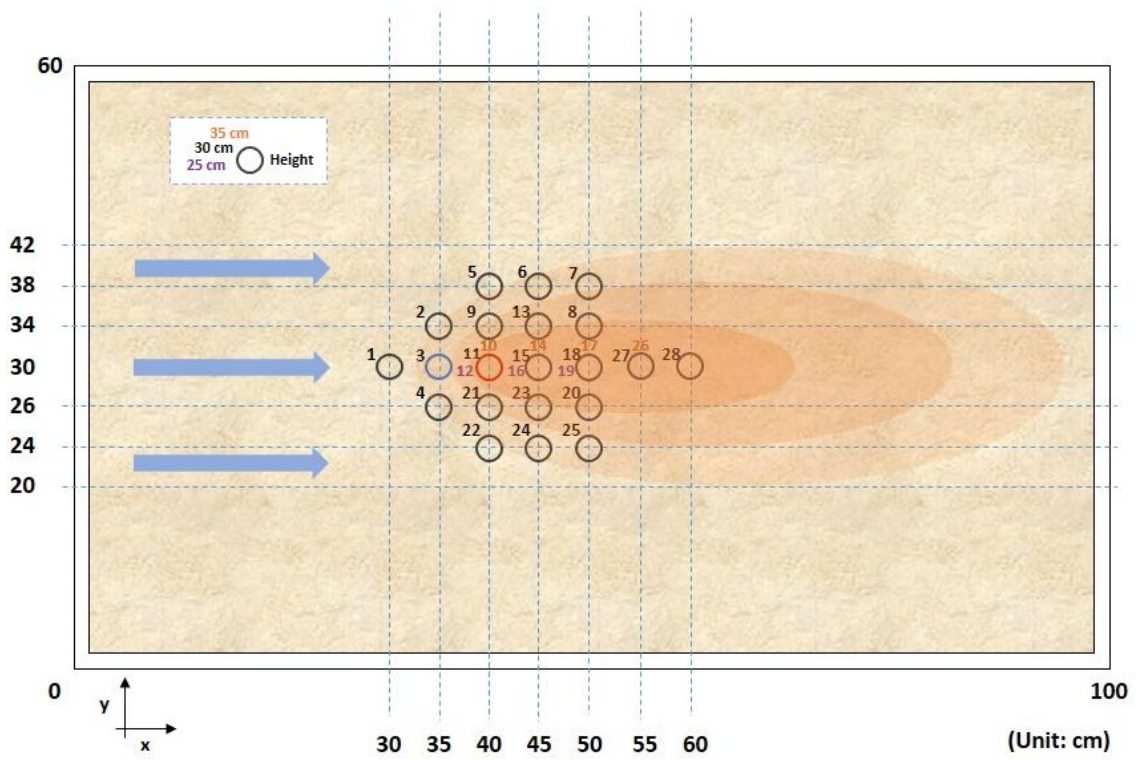
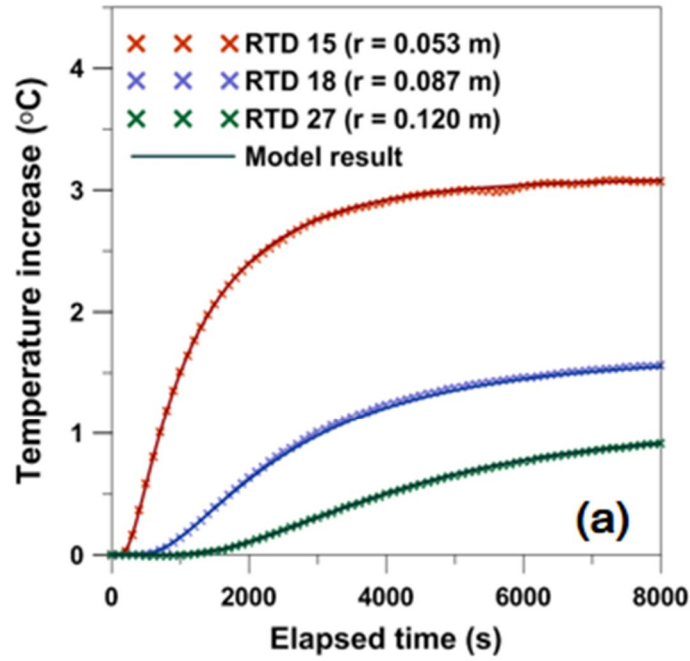


Fig. 4-4. Concept of the heat tracer test with regional flow and the heat transfer process based on heat dispersion and heat convection (thermal plume described as orange elliptical circles).

Heat tracer test with $q = 1.96$ m/d



Heat tracer test with $q = 3.21$ m/d

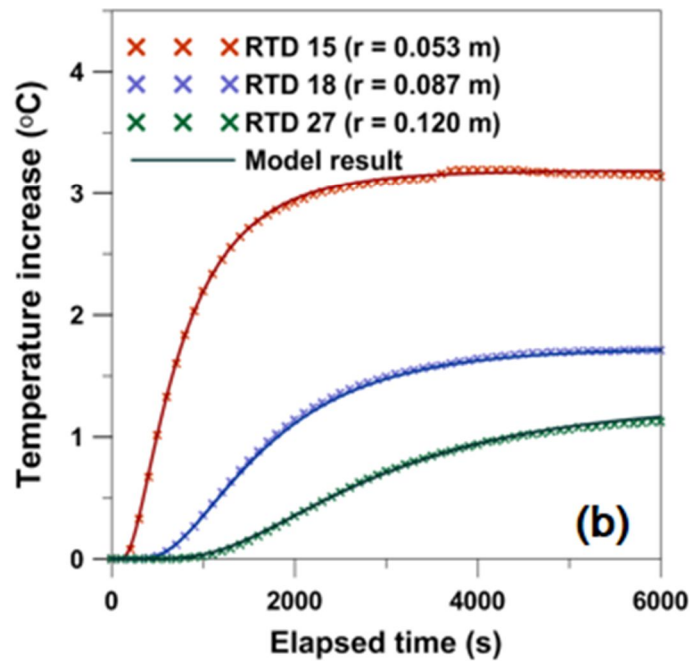
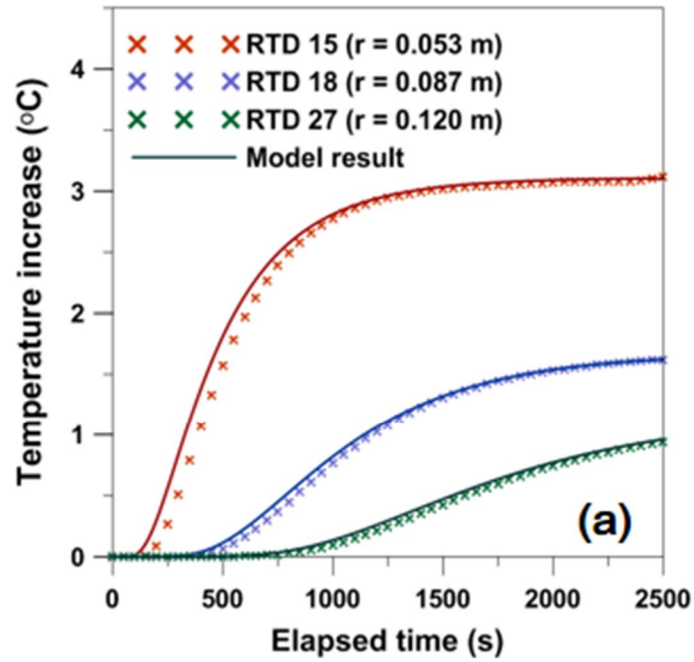


Fig. 4-5. The temperature breakthrough curves obtained by the measurements on center-line (in a cross-shape symbol) and the MCPS model results (in a solid line):
(a) flow condition of $q = 1.96$ m/d and (b) flow condition of $q = 3.21$ m/d.

Heat tracer test with $q = 5.46$ m/d



Heat tracer test with $q = 6.96$ m/d

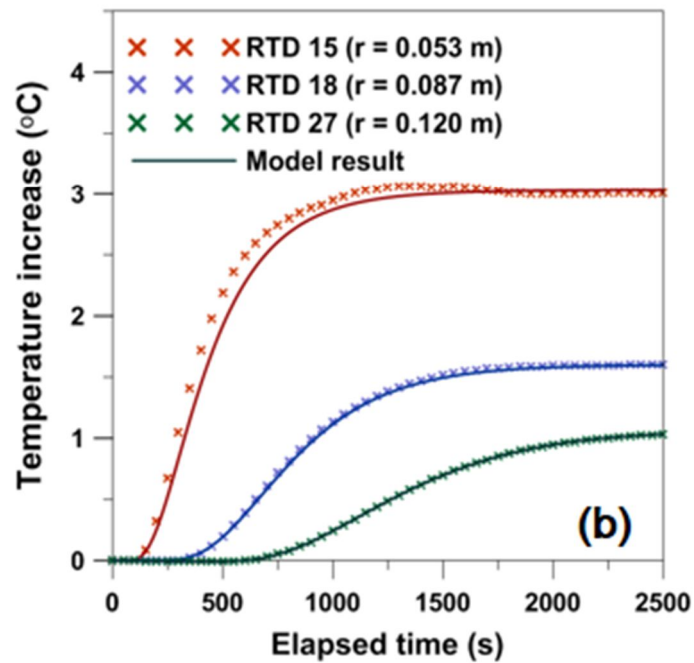
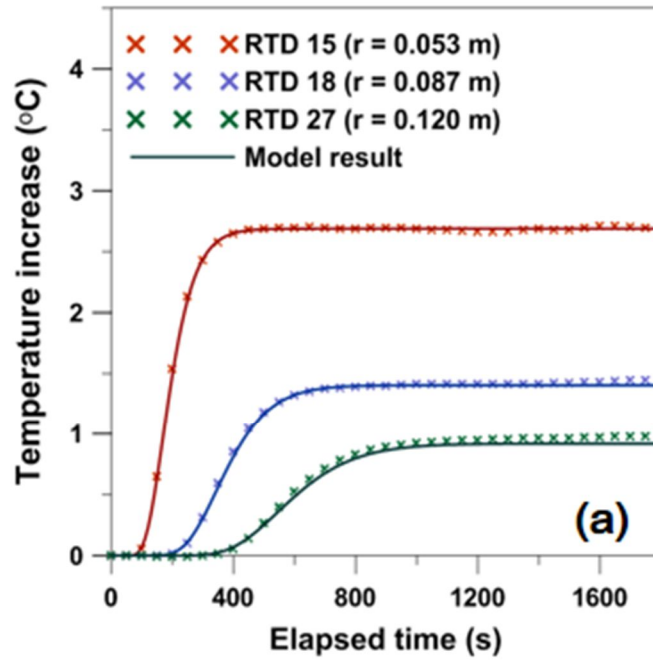


Fig. 4-6. The temperature breakthrough curves obtained by the measurements on center-line (in a cross-shape symbol) and the MCPS model results (in a solid line): (a) flow condition of $q = 5.46$ m/d and (b) flow condition of $q = 6.96$ m/d.

Heat tracer test with $q = 14.43$ m/d



Heat tracer test with $q = 19.46$ m/d

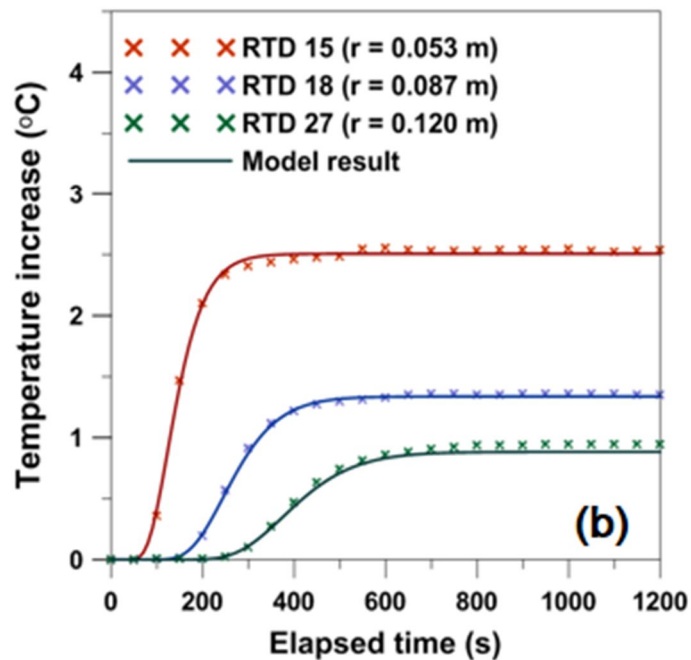
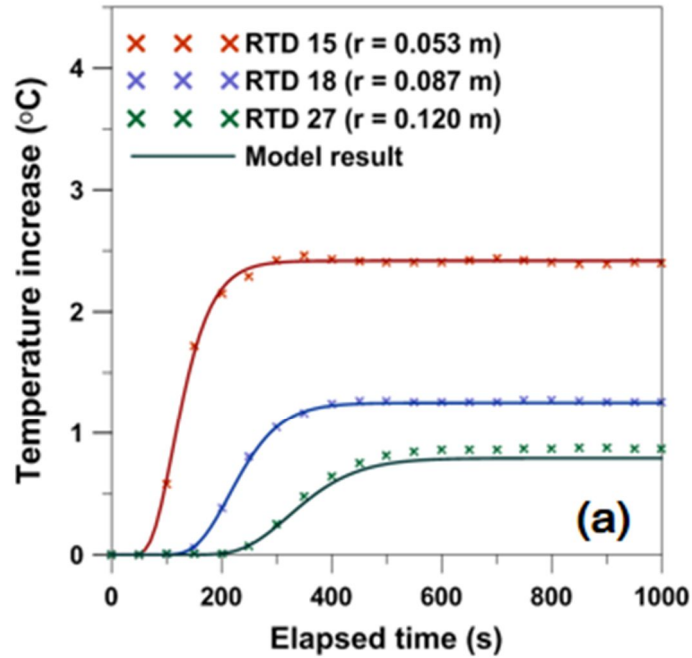


Fig. 4-7. The temperature breakthrough curves obtained by the measurements on center-line (in a cross-shape symbol) and the MCPS model results (in a solid line):
(a) flow condition of $q = 14.43$ m/d and (b) flow condition of $q = 19.46$ m/d.

Heat tracer test with $q = 21.78$ m/d



Heat tracer test with $q = 23.62$ m/d

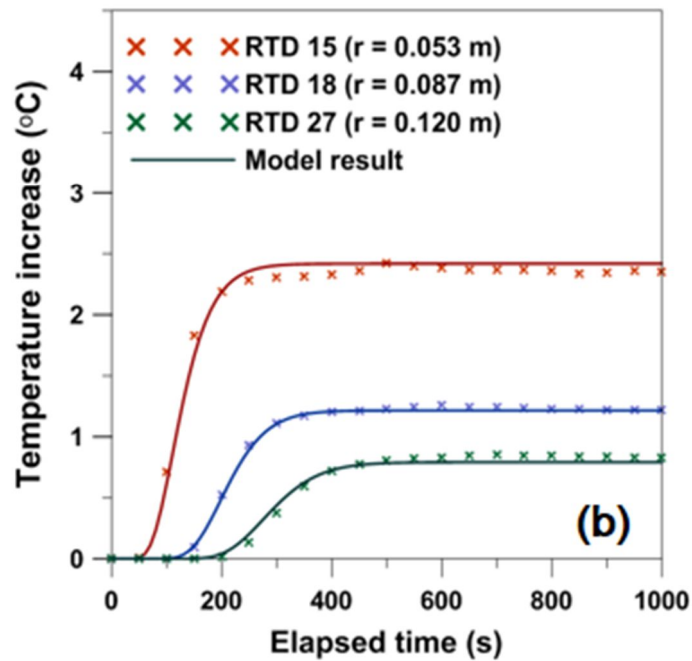
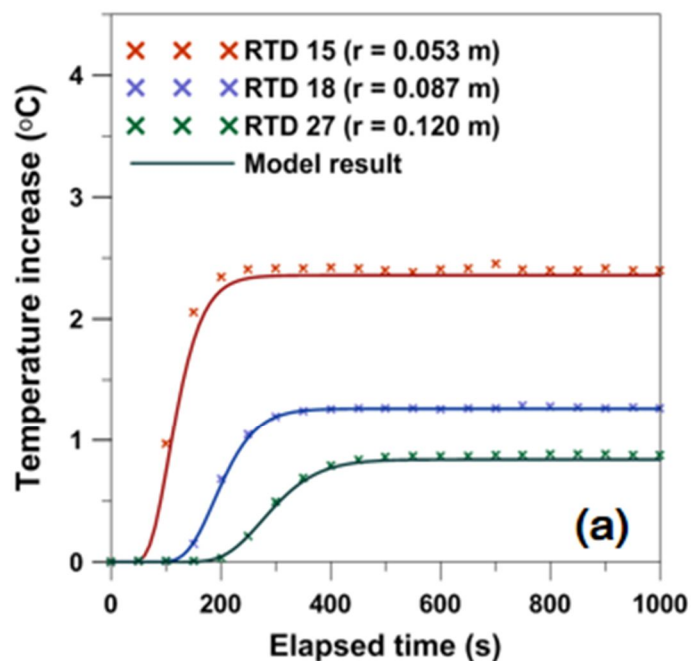


Fig. 4-8. The temperature breakthrough curves obtained by the measurements on center-line (in a cross-shape symbol) and the MCPS model results (in a solid line): (a) flow condition of $q = 21.78$ m/d and (b) flow condition of $q = 23.62$ m/d.

Heat tracer test with $q = 25.44$ m/d



Heat tracer test with $q = 26.14$ m/d

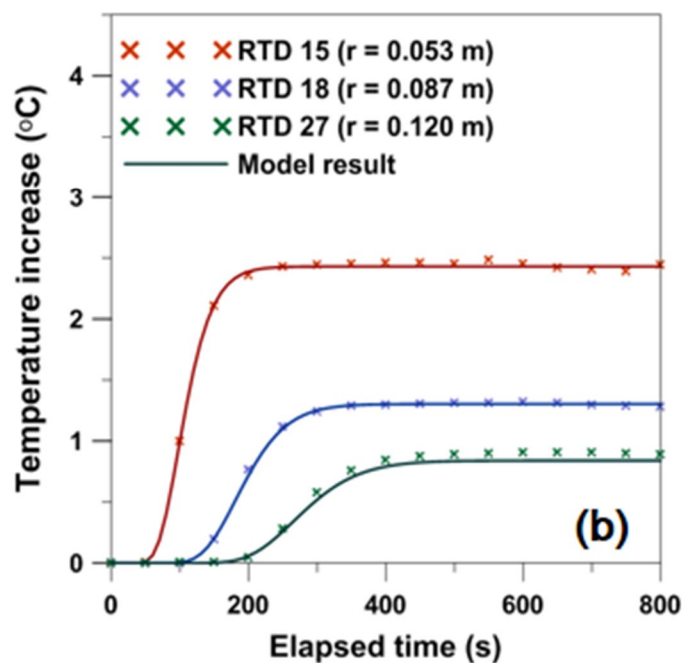


Fig. 4-9. The temperature breakthrough curves obtained by the measurements on center-line (in a cross-shape symbol) and the MCPS model results (in a solid line): (a) flow condition of $q = 25.44$ m/d and (b) flow condition of $q = 26.14$ m/d.

Table 4-2. Thermal dispersion coefficients and thermal front velocity derived from the best fit between measurements and the model

Flow condition (q)		1.96 m/d	3.21 m/d	5.46 m/d	6.96 m/d	14.43 m/d	19.46 m/d	21.78 m/d	23.62 m/d	25.44m/d	26.14 m/d
$D_{L,t}$ [m ² /s]	RTD 15	8.75×10^{-7}	9.75×10^{-7}	1.19×10^{-6}	9.66×10^{-7}	8.47×10^{-7}	1.25×10^{-6}	1.37×10^{-6}	1.30×10^{-6}	1.25×10^{-6}	1.16×10^{-6}
	RTD 18	7.18×10^{-7}	7.63×10^{-7}	8.53×10^{-7}	7.80×10^{-7}	8.70×10^{-7}	1.19×10^{-6}	1.17×10^{-6}	1.18×10^{-6}	1.20×10^{-6}	1.23×10^{-6}
	RTD 27	5.59×10^{-7}	7.79×10^{-7}	7.86×10^{-7}	6.31×10^{-7}	9.00×10^{-7}	1.16×10^{-6}	1.24×10^{-6}	1.25×10^{-6}	1.31×10^{-6}	1.31×10^{-6}
$D_{T,t}$ [m ² /s]	RTD 15	8.54×10^{-7}	8.29×10^{-7}	8.51×10^{-7}	8.73×10^{-7}	9.86×10^{-7}	1.06×10^{-6}	1.10×10^{-6}	1.12×10^{-6}	1.09×10^{-6}	1.09×10^{-6}
	RTD 18	9.09×10^{-7}	8.61×10^{-7}	8.90×10^{-7}	9.30×10^{-7}	1.06×10^{-6}	1.12×10^{-6}	1.19×10^{-6}	1.23×10^{-6}	1.18×10^{-6}	1.14×10^{-6}
	RTD 27	1.24×10^{-7}	1.02×10^{-6}	1.12×10^{-6}	1.25×10^{-6}	1.36×10^{-6}	1.40×10^{-6}	1.48×10^{-6}	1.55×10^{-6}	1.48×10^{-6}	1.44×10^{-6}
v^t [m/s]	RTD 15	3.6×10^{-5}	5.9×10^{-5}	1.0×10^{-4}	1.3×10^{-4}	2.6×10^{-4}	3.5×10^{-4}	4.0×10^{-4}	4.3×10^{-4}	4.6×10^{-4}	4.8×10^{-4}
	RTD 18	3.3×10^{-5}	5.4×10^{-5}	9.2×10^{-5}	1.2×10^{-4}	2.4×10^{-4}	3.3×10^{-4}	3.7×10^{-4}	4.0×10^{-4}	4.3×10^{-4}	4.4×10^{-4}
	RTD 27	4.0×10^{-5}	6.5×10^{-5}	1.1×10^{-4}	1.4×10^{-4}	2.9×10^{-4}	3.9×10^{-4}	4.4×10^{-4}	4.8×10^{-4}	5.1×10^{-4}	5.3×10^{-4}
NRMSE		0.0038	0.0079	0.0052	0.0064	0.0089	0.0122	0.0099	0.0119	0.0085	0.0102

* $D_{L,t}$: longitudinal thermal dispersion coefficient

$D_{T,t}$: transverse thermal dispersion coefficient

v^t : thermal front velocity

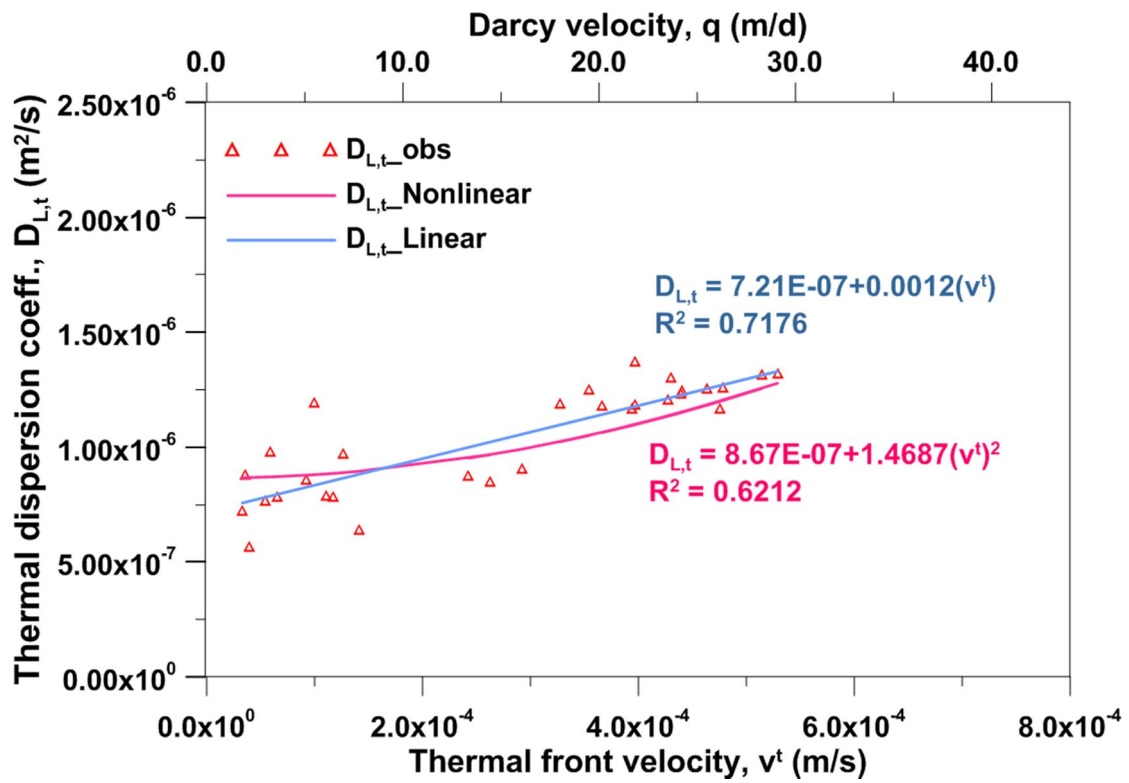


Fig. 4-10. The result of regression analyses for longitudinal thermal dispersion coefficients ($D_{L,t}$) and thermal front velocities (v^t) in this experiment. Linear increasing trend of $D_{L,t}$ with v^t (in a blue solid line) shows R^2 of 0.7176. Non-linear increasing trend of $D_{L,t}$ with v^t (in a red solid line) shows R^2 of 0.6212.

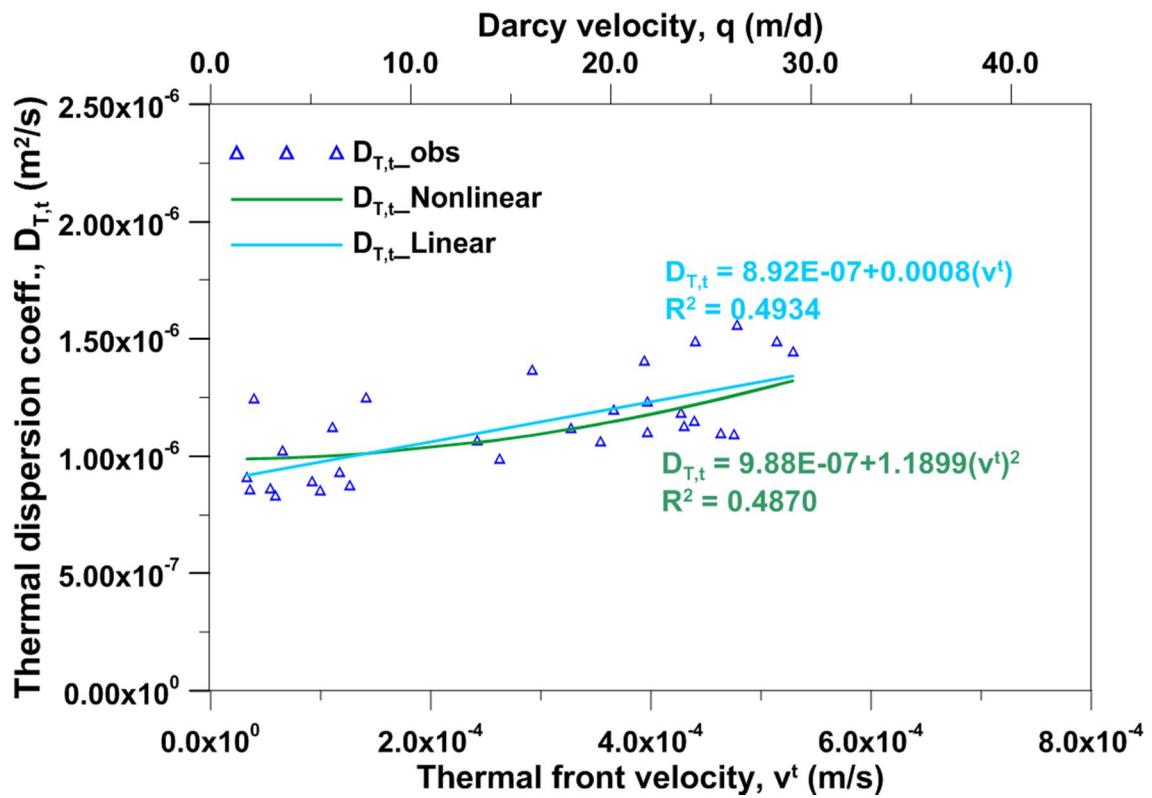


Fig. 4-11. The result of regression analyses for transverse thermal dispersion coefficients ($D_{T,t}$) and thermal front velocities (v^t) in this experiment. Linear increasing trend of $D_{T,t}$ with v^t (in a blue solid line) shows R^2 of 0.4934. Non-linear increasing trend of $D_{T,t}$ with v^t (in a red solid line) shows R^2 of 0.4870.

4.3 Heat tracer tests with water injection under various flow conditions

4.3.1 Laboratory experiments and model validation

Lab-scale heat tracer tests with injection of warmed water were performed under the same flow conditions as tests using a resistor to compare the thermal dispersion behavior in the disturbed groundwater environment with one in the natural groundwater environment. Because it was impossible to place the injection point at the exactly same location as the resistor, the injection well was installed 4.53 cm away to the left from the resistor, but still on the same x-axis. Therefore, the concept of tests is the same as section 4.2 except that the heat source is warmed water flowing through 2 cm-wide screen of the injection well located a few centimeters away on the left side from the resistor. Heat flow rate (Q_{heat}) from the injected water is determined as $Q_{\text{heat}} [\text{W}] = Q_{\text{water}} [\text{ml/s}] \times \rho_w c_w [\text{J/ml/K}] \times \Delta T [\text{K}]$. Before the heat tracer test was carried out, tests to determine injection rate (Q_{water}) and temperature increment (ΔT) were proceeded. Considering that there is a minimum injection rate allowing injected water to run outwards through the well screen and to flow continuously, injection rates of 35 ml/min, 50 ml/min, and 70 ml/min were determined for this experiment. Although temperature increment of injected water (ΔT) was not consistent in every test due to the sensitivity issue of the thermostat, all the temperature increments were determined not to exceed 3 K to prevent the density effect. In order to provide the same flow condition as heat tracer tests using the resistor, test with water injection was performed right after the background temperature in the porous medium had been recovered from the test using resistor. The injection heat tracer test with certain flow velocity was repeated either twice (35 and 70 ml/min) or three times (35, 50, and 70 ml/min) with different injection

rates suggested above to investigate the influence of injection rate on thermal dispersion behavior.

The experimental results were used to validate the numerical model. In numerical simulations for the validation, thermal parameters derived from section 4.1 and 4.2 were used (Table 4-3). The groundwater flow conditions were designed as same as the experiments. To simulate the injection of warmed water, transient temperature data of injected water was directly inserted in the model as time-variant Dirichlet condition. Injection rates were set as mentioned above. Fig.4-12 shows the comparison of the experimental results and the simulation results at observation points ($r = 0.10$ and 0.15 m) under (a) $q = 3.21$ m/d and (b) $q = 6.96$ m/d as examples. The difference is within 0.3 °C and 0.1 °C respectively, which indicates a reasonable agreement between the measured and numerical data. Thus, the numerical model can be used to simulate the movement of thermal plume and the thermal dispersion behavior under forced groundwater flow caused by water injection.

Table 4-3. Thermal properties used in numerical simulations (other design parameters: pre-determined in section 3.2.2)

Parameters	Symbol	Unit	Value
Volumetric heat capacity of solid*	$\rho_s c_s$	$10^6 \text{ J/m}^3\text{-K}$	1.904
Thermal conductivity of solid*	κ_s	W/m-K	3.339
Longitudinal thermal dispersivity**	β_L	10^{-3} m	1.15
Transverse thermal dispersivity**	β_T	10^{-3} m	0.90

*Values were derived from heat tracer tests using a resistor (see section 4.1 and 4.2).

**Values were derived from the regression analyses of longitudinal/transverse thermal dispersion coefficients estimated in section 4.2.

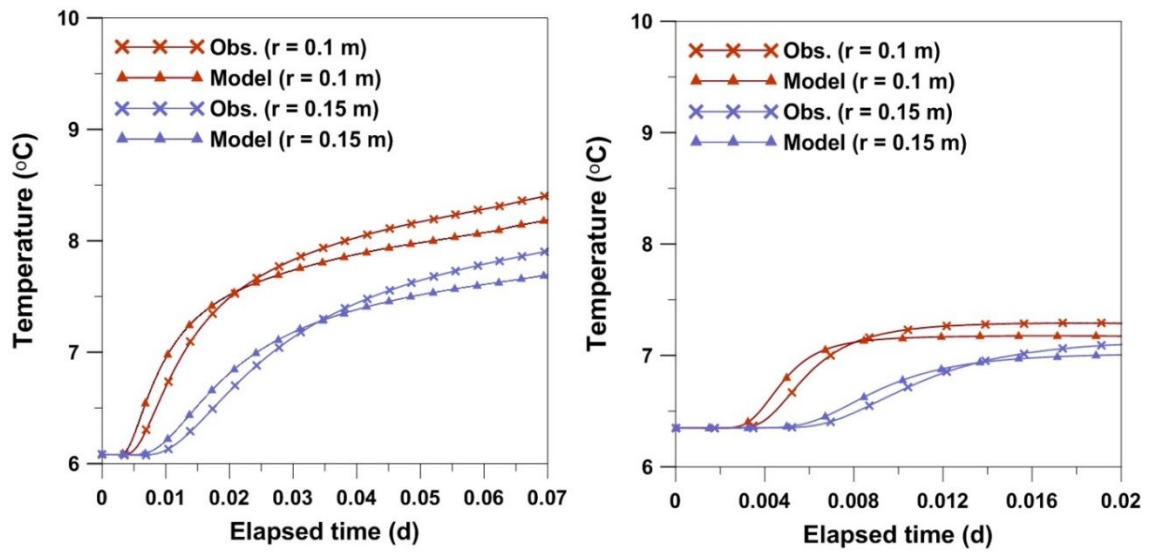


Fig. 4-12. Comparison of the temperature data obtained from the numerical simulation (in triangle) with that from the experiment (in x-shape) at observation points ($r = 0.10$ and 0.15 m): (a) heat tracer test under $q = 3.21$ m/d and $Q_{\text{water}} = 70$ ml/min, (b) heat tracer test under $q = 6.96$ m/d and $Q_{\text{water}} = 70$ ml/min.

4.3.2 Numerical simulations with various regional flow velocities and injection rates

Numerical simulations using the validated model were conducted for total 24 cases with different regional flow velocities and injection rates. The purpose of the case simulation was (i) to fairly compare the thermal dispersion behavior in the forced flow environment caused by water injection with that in the natural flow environment and (ii) to investigate the degree of disturbance in flow field and its influence on the thermal dispersion behavior depending on different flow and injection rates. Table 4-4 shows the condition applied in each case simulation. Hydraulic gradients were adjusted from 0.025 to 0.150 (case A – case F) generating regional flow velocities from 5.05 – 30.33 m/d. Injection rates were controlled from 0.100 m³/d to 0.025 m³/d (case 1 – case 4). In Fig.4-13, the temperature response data at an observation point ($x = 0.45$ m; $r_{inj-obs} = 0.10$ m, see Fig.3-20) obtained from the simulation case A and F (in green color) are compared with the data obtained from simulation where the same amount of heat was supplied by a small heater (in orange color). Although the same heat flux was fed through from the source point, the gap between simulations with and without injection distinctly occurred due to the disturbance in the flow field. To be more specific, disturbed flow in with-injection-simulations caused lower temperature increase and earlier arrival time of thermal plume at the observation points. Also, this difference increased with injection rate in all cases. This indicates that higher injection rate induces more disturbance in groundwater flow field which leads to more dissipation of thermal plume. In addition, the difference seems to decrease when the regional groundwater flow velocity becomes higher. NRMSE (Normalized RMSE; RMSE divided by temperature increment, ΔT) between simulation results with and without injection for all

24 cases also supports the result that the gap between two increases with injection rate and decreases with regional flow velocity (Fig.4-14).

As mentioned above, the movement of thermal plume is different when the heat is supplied by a heater from when the same amount of heat is supplied by injection of warmed water because of the disturbed flow field generated by water injection. An example of flow velocity field along the center-line parallel to the x-axis displays the drastic increase in flow velocity around the injection point (Fig.4-15). To explain the NRMSE trends in case simulations (see Fig.4-14) with velocity disturbance, the ratio of velocity increase at observation points to the regional flow velocity was calculated for all the cases (Fig.4-16). The degree of disturbance in flow velocity increases with injection rate and decreases with regional flow velocity, which accords with the NRMSE trends. Subsequent calculation was carried out on the ratio of change in thermal dispersion coefficients (longitudinal/transverse; $D_{L,T,t}$) attributed to the disturbance in flow velocity field (Fig.4-17). At the observation located 10 cm away from the injection point ($x_{obs} = 0.45$ m), longitudinal thermal dispersion coefficient ($D_{L,t}$) increased up to 6.32 % compared to undisturbed flow field when the regional flow velocity is lowest and the injection rate is highest. This not only suggests that forced flow field by water injection enlarges the magnitude of thermal dispersion but also implies that thermal dispersion term can play a noticeable role in navigating the thermal plume movement in forced flow fields.

Table 4-4 Case simulations with different hydraulic gradient (or flow velocity) and injection rate

Case	A	B	C	D	E	F
Hydraulic gradient	0.025	0.050	0.075	0.010	0.125	0.150
(Flow velocity, m/d)	(5.05)	(10.11)	(15.16)	(20.22)	(25.27)	(30.33)
1	$Q_{\text{water}} = 0.100 \text{ m}^3/\text{d}, \Delta T = 1.5 \text{ K}, Q_{\text{heat}} = 7.30 \text{ W}$					
2	$Q_{\text{water}} = 0.075 \text{ m}^3/\text{d}, \Delta T = 1.5 \text{ K}, Q_{\text{heat}} = 5.47 \text{ W}$					
3	$Q_{\text{water}} = 0.050 \text{ m}^3/\text{d}, \Delta T = 1.5 \text{ K}, Q_{\text{heat}} = 3.65 \text{ W}$					
4	$Q_{\text{water}} = 0.025 \text{ m}^3/\text{d}, \Delta T = 1.5 \text{ K}, Q_{\text{heat}} = 1.82 \text{ W}$					

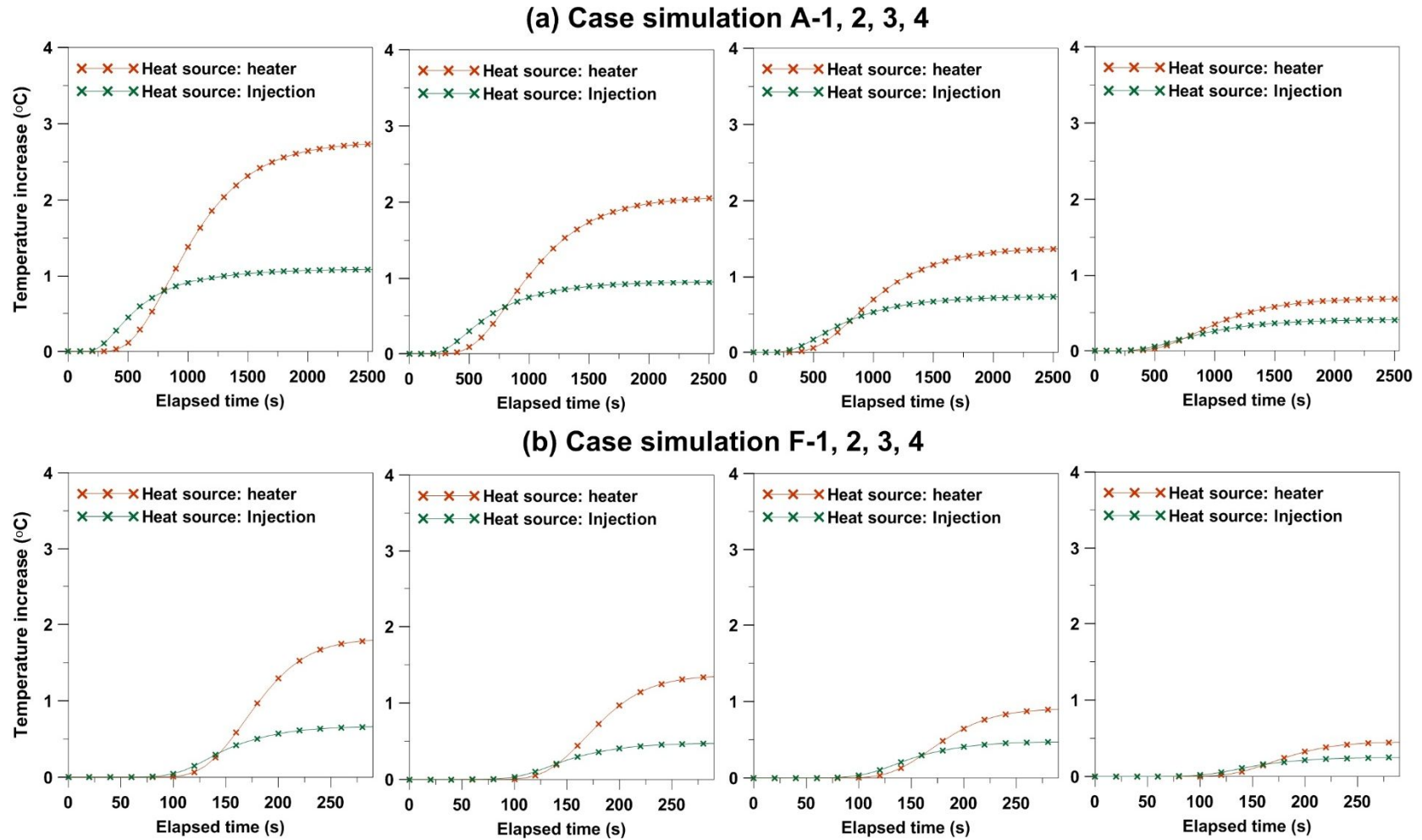


Fig. 4-13. The temperature response data at $x_{\text{obs}} = 0.45 \text{ m}$ ($x_{\text{inj}} = 0.35 \text{ m}$) obtained from heat tracer test simulations with (in a green symbol) and without (in a red symbol) water injection under (a) lowest flow condition (case A) and (b) highest flow condition (case F).

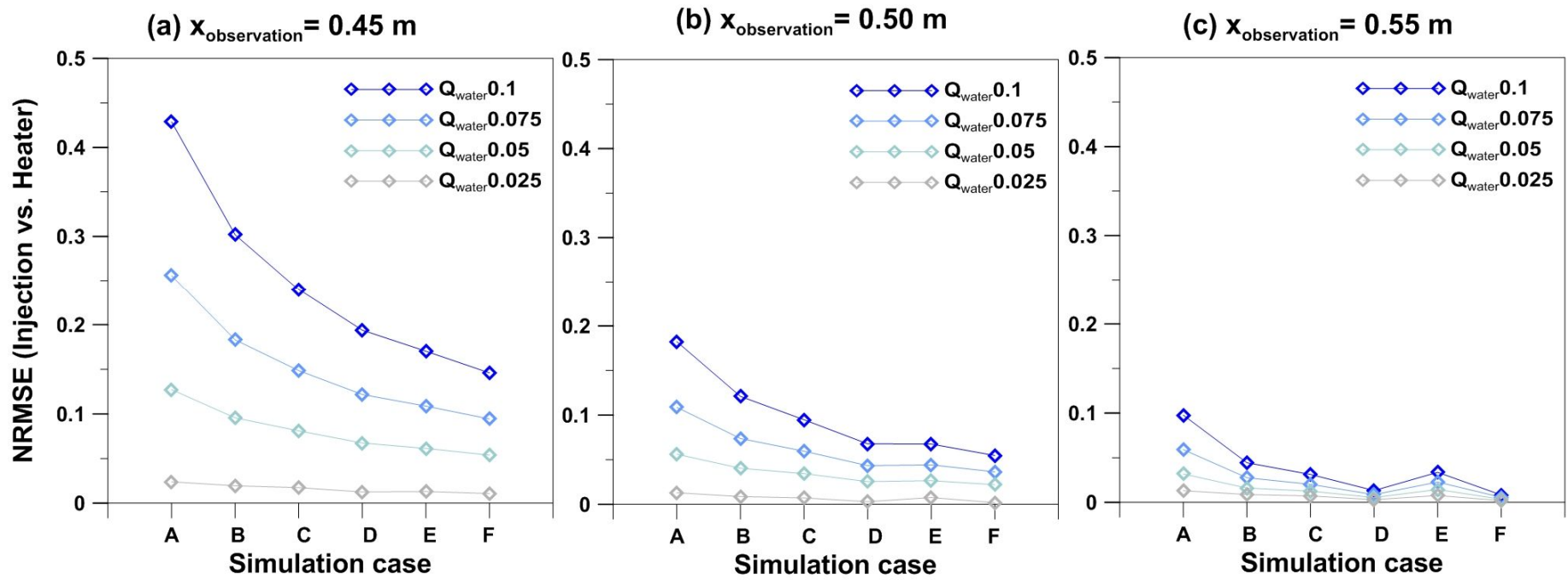


Fig. 4-14. NRMSE between temperature data resulted from simulation with and without water injection for all 24 cases obtained at 3 observation points: (a) $x_{\text{obs}} = 0.45$ m, (b) $x_{\text{obs}} = 0.50$ m, (c) $x_{\text{obs}} = 0.55$ m ($x_{\text{inj}} = 0.35$ m).

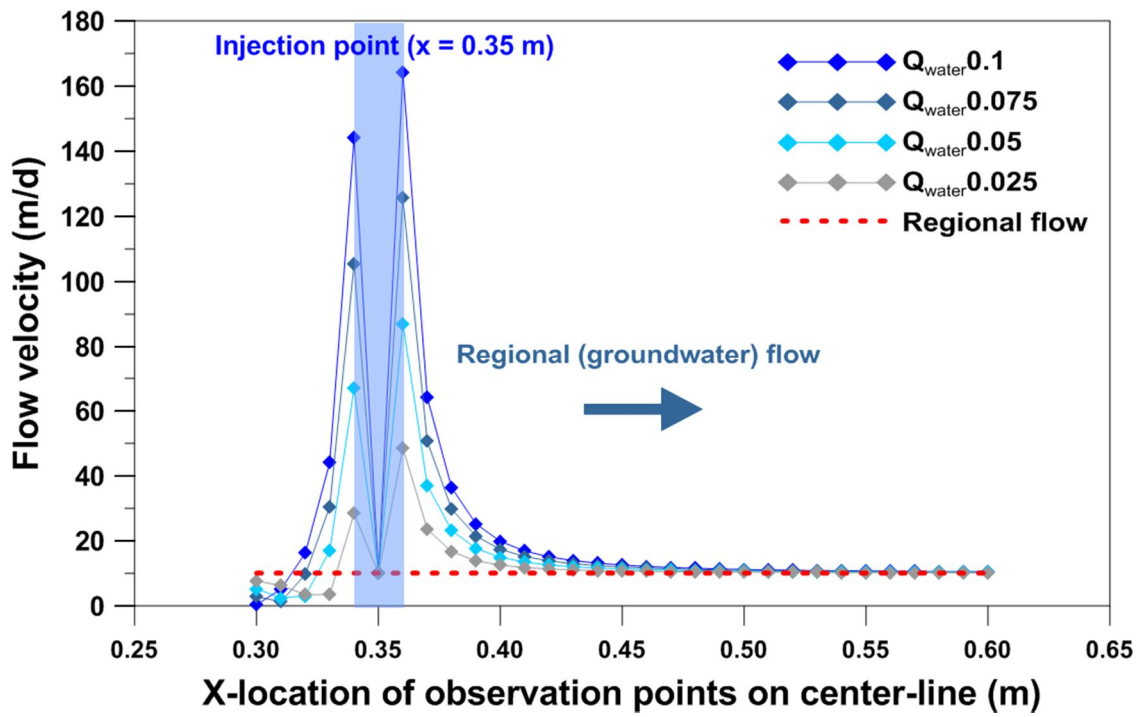


Fig. 4-15. Flow velocity field along the center-line ($x = 0\sim 1$ m, $y = 0.3$ m, $z = 0.3$ m) depending on the injection rate in simulation case B.

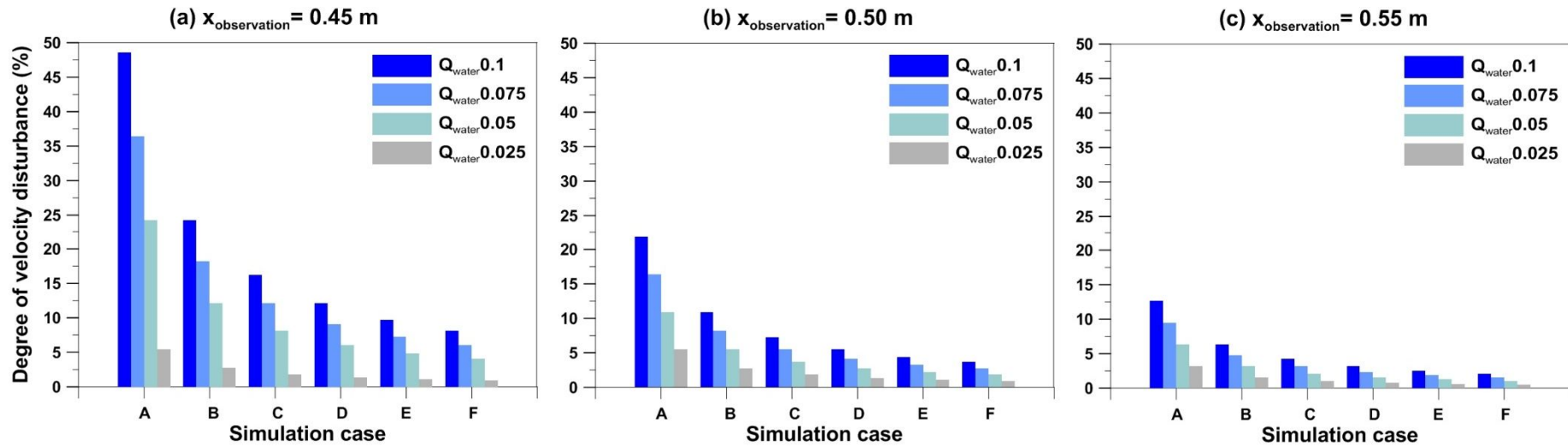


Fig. 4-16. The ratio (or degree) of flow velocity increase (or disturbance) at three observation points (a-c) for 24 cases.

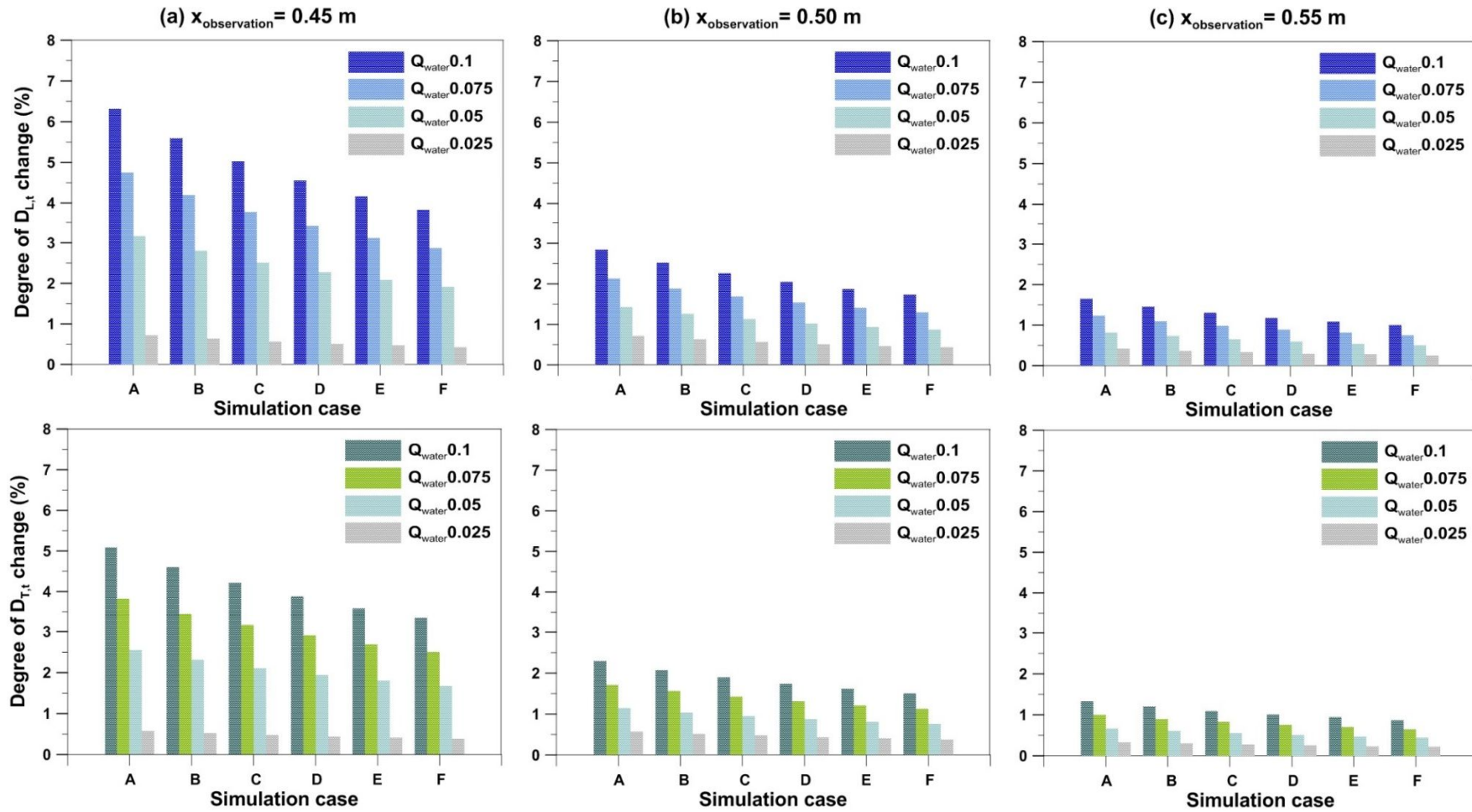


Fig. 4-17. The ratio of change in longitudinal (above) and transverse (below) thermal dispersion coefficients arisen from the disturbed flow velocity field by injection for 24 cases.

4.4 Discussions

4.4.1 Dependence of thermal dispersion coefficient on thermal front velocity

As mentioned above, regression analysis of the parameters derived from heat tracer tests using a resistor resulted in both acceptable linear and non-linear increasing trends of longitudinal thermal dispersion coefficient ($D_{L,t}$) with thermal front velocity (v^t). However, the linear increasing trend showed higher coefficient of determination ($R^2 = 0.718$) while the non-linear increasing trend showed slightly lower coefficient ($R^2 = 0.621$) (Fig.4-10). Thermal Peclet number which decides whether the heat transport in porous medium is conduction dominant or convection dominant is defined as (de Marsily, 1986; Anderson, 2005),

$$Pe^t = \frac{\rho_w c_w q L}{\kappa_0} \quad (\text{Eq.4-1})$$

where L is a characteristic length [m] that is usually replaced with the mean grain size (d_{50}) of the porous medium. Thermal Peclet numbers estimated from the heat tracer tests using a resistor were below 1, which means heat transport conditions in this experiment are conduction dominant. This explains why the longitudinal thermal dispersion coefficient ($D_{L,t}$) in this experiment represented both linear increase and non-linear increase with thermal front velocity without large dominance in one trend.

Non-linear relationship between $D_{L,t}$ and v^t suggested by the first meaningful lab-scale experiment on thermal dispersion coefficient has been validated in convection-dominated flow conditions ($Pe^t > 10$) (Green et al., 1964; Levec and Carbonell, 1985b; Metzger et al., 2004; Testu et al., 2007). On the other hand, experiments under relatively low flow conditions either revealed a linear increasing trend of $D_{L,t}$ with critical deviation or found no distinct trend within acceptable range of R^2 (Yagi et al., 1960;

Kunii and Smith, 1961). Although Rau et al. (2012) recently suggested a square relationship of $D_{L,t}$ with v^t after performing lab-scale heat tracer tests under experimental conditions of $Pe^t < 2.5$, it was pointed out that the square relationship was distinct only within the range of $0.5 < Pe^t < 2.5$ and $D_{L,t}$ for $Pe^t < 0.5$ showed insignificant dependency on velocity.

Despite the flow conditions in this study being limited to conduction-dominated flow environment ($Pe^t < 1$) due to the limitations of the experimental device, a linear relationship between $D_{L,t}$ and v^t was derived with much less experimental scatter compared to the previous studies (Yagi et al., 1960; Kunii and Smith, 1961). It is noticeable that the obvious dependency of $D_{L,t}$ on v^t (or q) was observed in the sand material close to the natural porous medium and in the low flow conditions ($Re < 1$) which represent general groundwater environments, considering that related studies mostly have been using glass beads and simulating high flow conditions. However, since non-linear relationship which is in good agreement with the result of Rau et al. (2012) also showed recognizable R^2 value, further experimental investigation needs to be carried on by improving experimental device to examine the relationship of $D_{L,t}$ with v^t throughout the whole range of flow conditions (maybe $Re < 2.5$) that occurs in aquifers (Fig. 4-18).

For the transverse thermal dispersion coefficient ($D_{T,t}$), a linear increasing trend with $R^2 = 0.493$ and a non-linear increasing trend with $R^2 = 0.487$ (Fig.4-11) were revealed from regression analysis. This accords with the result of Rau et al. (2012) in that R^2 value of increasing trends in $D_{T,t}$ is lower than that in $D_{L,t}$ because of critical data scatter. However, R^2 values themselves were relatively higher in this study. These reliable regression analysis results for $D_{L,t}$ and $D_{T,t}$ provided firm input values of

thermal dispersivities ($\beta_{L,t}$ and $\beta_{T,t}$) that mirror the properties of porous medium used in the experiment. Thus, fair comparisons between heat transport simulations with and without water injection were conducted based on them.

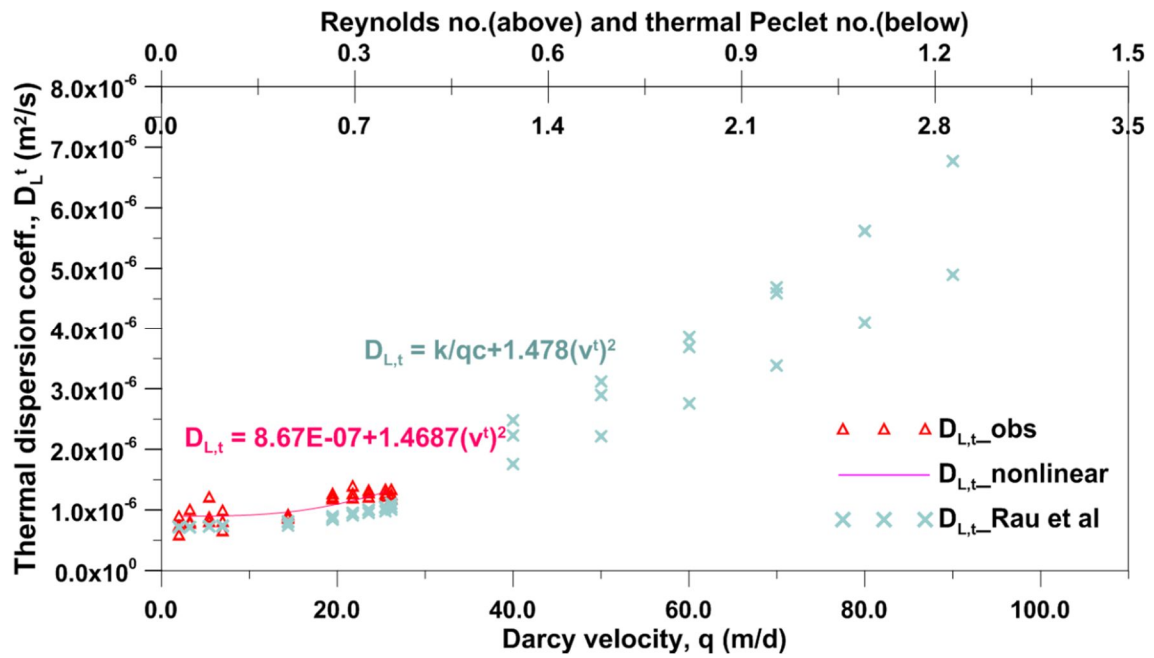


Fig. 4-18. Comparison between non-linear increasing trend resulted from this study and one resulted from Rau et al. (2012). The flow conditions were limited below $Pe^t = 1$ in this study.

4.4.2 Increase of thermal dispersion coefficients in heat transport under water injection

Increase of thermal dispersion coefficients ($D_{L/T,t}$) in with-injection simulations compared to without-injection ones shows that the disturbance in flow velocity field forced by water injection contributes to enlargement of the magnitude and the significance of thermal dispersion term. Especially in substantially conduction-dominated conditions, the increase in $D_{L/T,t}$ due to water injection becomes more substantial. Therefore, over/under-estimation of thermal dispersion coefficients can arouse significant errors in assessing the heat transport under water injection. Some might think that the increase of $D_{L/T,t}$ derived in this study is small enough to neglect. However, applying the result into field-scale heat transport brings the risk of overlooking thermal dispersion term onto a different level.

The mathematical description on thermal dispersion coefficients derived from section 4.2 and also embedded in the numerical model (FEFLOW) in section 4.3 includes thermal dispersivity ($\beta_{L/T}$; see Eq.2-6) which depends on the heterogeneity of physical properties in aquifer. Because of the significant heterogeneity of physical and thermal properties existing in field, $\beta_{L/T}$ applied for field-scale heat transport have larger values with a wider range (Neuman, 1990; Schulze-Makuch, 2005; Ferguson, 2007; Molina-Giraldo et al., 2011; Stauffer et al., 2014). Thus, the same ratio of increase in thermal dispersion can have bigger influence on the thermal plume movement under water injection in fields. Furthermore, using default values or reference values for thermal dispersion term without any consideration can lead to a bigger error in interpreting field-scale heat tracer tests with water injection. In order to reveal the error that can occur if different thermal dispersivity ($\beta_{L/T}$) was considered in heat tracer tests

with injection, numerical simulations for Case A-1 with 1, 10 and 10^2 times of $\beta_{L/T}$ (= 0.00115 m, see table 4-3) were carried out (Fig.4-19). The comparison of temperature response data shows that inappropriate adoption of thermal dispersion value could cause over/under-estimation of temperature increase at an observation point.

In assessing thermal risk (e.g. thermal feedback/recycling) in GWHP system to design the optimal one, it has been common that default thermal dispersivity or solute dispersivity replaces the real thermal dispersivity reflecting the aquifer properties. However, as Park et al. (2015) claimed in their research, over/under-estimation of thermal dispersion coefficients ($D_{L/T,t}$) attributed to the mistaken thermal dispersivity ($\beta_{L/T}$) can result in wrong thermal risk assessment. In this study, it was observed that the significance of thermal dispersion coefficient becomes larger in lower groundwater flow conditions with higher injection rates. Since groundwater flow conditions stay within a low velocity range ($Re < 1$) in numerous cases and pumping/injection rates are designed very high in general GWHP systems, thermal dispersion coefficient should not be overlooked in evaluating heat transport in GWHP systems.

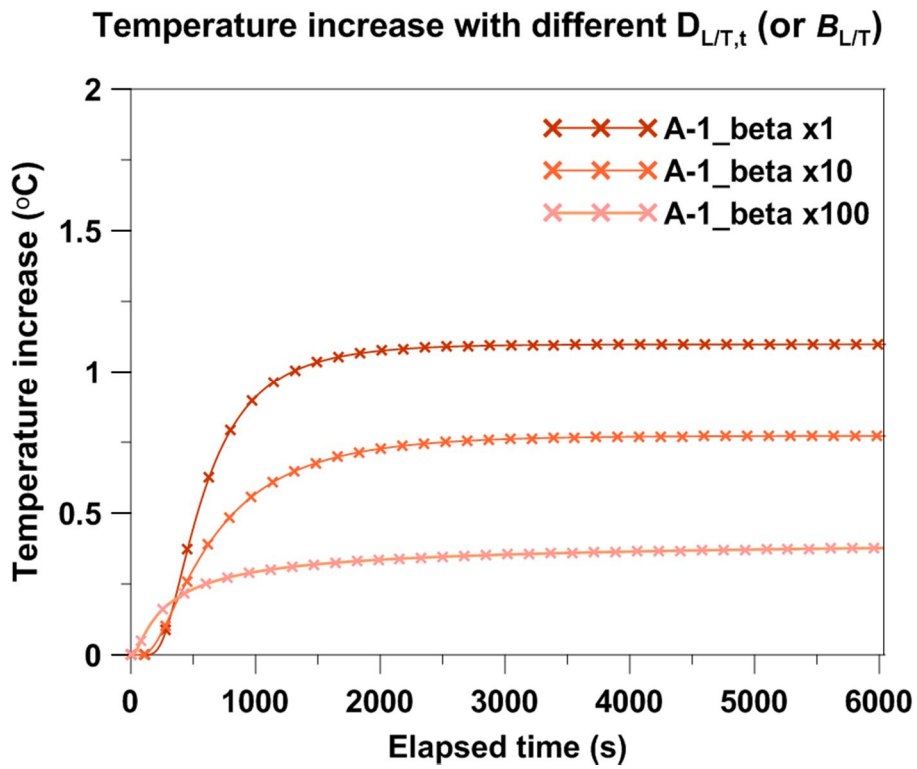


Fig. 4-19. Temperature breakthrough curves obtained from case A-1 simulations with different ($\times 1$, $\times 10$, and $\times 100$) thermal dispersivities ($\beta_{L/T}$). The observation point was one located at $x = 0.45$ m; $r_{inj-obs} = 0.10$ m.

5 Conclusion

Although it is known that thermal dispersion shows a greater impact on heat transport mechanism with increasing flow velocities, thermal dispersion term has been rarely focused as an influential factor in evaluating heat transport in GWHP systems where high flow condition is usually induced. In addition, previous experimental studies on thermal dispersion behavior lack their applicability in thermal dispersion under forced groundwater flow because they are limited to natural groundwater flow environment. These aroused the necessity of experimental investigation on thermal dispersion behavior under the forced flow condition as conducted in this study. Because lab-scale experiments allow more thorough study on thermal dispersion term by adjusting other physical factors, a laboratory device to simulate the heat transport in groundwater environment was designed in this research. Two different heat sources: (a) a resistor and (b) injection of warmed water were used in lab-scale heat tracer tests to compare the thermal dispersion behavior in forced flow conditions with that in natural flow conditions.

Experimental results from heat tracer tests using a small resistor under no flow were first performed to estimate the thermal properties of porous medium and the correct location of sensors. This provided the subsequent estimation of thermal dispersion term with better reliability. Results from heat tracer tests using a small resistor with various regional flow velocities exhibited linear dependency of thermal dispersion coefficient on thermal front velocity (or flow velocity) with slightly higher R^2 than nonlinear dependency probably because the flow condition in the experiment stayed within conduction-dominant range. However, it is noticeable that obvious dependency of thermal dispersion coefficient was observed even in the low flow

conditions and in the sand material close to the natural porous medium considering previous studies with glass beads and low flow velocities ended up with unclear trends and critical scatters. Also, computed linear regression coefficient provided a firm input value for thermal dispersivity in numerical simulations and allowed reasonable comparison between thermal dispersion in forced flow with that in natural flow. On the other hand, potential possibility in non-linear dependency that accords with some previous researches could be examined by performing further experiments with improved device.

Numerical case-simulations using the numerical model validated with results from heat tracer tests using injection of warmed water were carried out to estimate the change in thermal dispersion under forced flow conditions depending on regional flow velocity and injection rate. The analysis results indicated that thermal dispersion coefficients increased due to disturbance in flow velocity field around injection point compared to undisturbed flow environment. The degree of increase was largest with the lowest regional flow velocity and the highest injection rate. Even though the increase ratio might be considered small enough to neglect, the influence of the same increase in field-scale thermal dispersion on thermal plume movements can be larger because the field thermal dispersion is higher by ten to thousand times. Therefore, irrational adoption of default or reference thermal dispersion values, which has been common when designing GWHP systems and analyzing field heat tracer tests using water, can cause substantial error in predicting thermal plume movement. In particular, according to the results of this research, the error can be more significant when groundwater flow is low and injection rate is high which normally happens in GWHP systems. Thus, thermal dispersion term should not be disregarded in evaluating the heat transport under forced

groundwater flow conditions caused by water injection.

6 References

- Anderson, M.P., 2005, Heat as a ground water tracer, *Groundwater*, 43(6), 951-968.
- Balland, V. and Arp, P.A., 2005, Modeling soil thermal conductivities over a wide range of conditions, *Journal of Environmental Engineering Science*, 4, 549-558.
- Banks, D., 2009, Thermogeological assessment of open-loop well-doublet schemes: a review and synthesis of analytical approaches, *Hydrogeology Journal*, 17, 1149-1155.
- Bear, J., 1972, *Dynamics of fluids in porous media*, Elsevier, NY, 764 p.
- Carslaw, H.S. and Jaeger, J.C., 1959, *Conduction of heat in solids*, Oxford University Press, NY, 520 p.
- Casasso, A. and Sethi, R., 2015, Modelling thermal recycling occurring in groundwater heat pumps (GWHPs), *Renewable Energy*, 77, 86-93.
- De Marsily, G., 1986, *Quantitative hydrogeology: groundwater hydrology for engineers*, Academic Press, SD, 440 p.
- Diersch, H.-J.G., 2005, *FEFLOW Reference Manual*, WASY GmbH, Berlin, Germany, 292 p.
- Ferguson, G., 2007, Heterogeneity and thermal modeling of groundwater, *groundwater*, 45(4), 485-490.
- Gao, Q., Zhou, X.Z, Jiang, Y., Chen, X.L., and Yan, Y.Y., 2013, Numerical simulation of the thermal interaction between pumping and injecting well groups, *Applied Thermal Engineering*, 51, 10-19.
- Green, D.W., Perry, R.H., and Babcock, R.E., 1964, Longitudinal dispersion of thermal energy through porous media with a flowing fluid, *Aiche Journal*, 10, 645–651.
- Kunii, D. and Smith, J.M., 1961, Heat transfer characteristics of porous rocks: II. Thermal conductivities of unconsolidated particles with flowing fluids, *American*

Institute of Chemical Engineers Journal, 7(1), 29-34.

Kwon, K.S., Lee, J.Y., and Mok, J.K., 2012, Update of current status on ground source heat pumps in Korea (2008-2011), The Geological Society of Korea, 48(2), 193-199. [in Korean]

Levec, J. and Carbonell, R.G., 1985, Longitudinal and lateral thermal dispersion in packed beds Part I: theory, Aiche Journal, 31, 581–590.

Lo Russo, S. and Civita, M.V., 2009, Open-loop groundwater heat pumps development for large buildings: a case study, Geothermics, 38, 335-345.

Lo Russo, S., Taddia, G., Baccino, G., and Verda, V., 2011, Different design scenarios related to an open loop groundwater heat pump in a large building: Impact on subsurface and primary energy consumption, Energy and Buildings, 43, 347-357.

Lu, X., Ren, T., and Gong, Y., 2009, Experimental investigation of thermal dispersion in saturated soils with one-dimensional water flow, Soil Science Society of America Journal, 73 (6), 1912–1920.

Metzger, T., Didierjean, S., and Maillet, D., 2004, Optimal experimental estimation of thermal dispersion coefficients in porous media, International Journal of Heat and Mass Transfer, 47, 3341–3353.

Molina-Giraldo, N., Bayer, P., and Blum, P., 2011, Evaluating the influence of thermal dispersion on temperature plumes from geothermal systems using analytical solutions, International Journal of Thermal Sciences, 50(7), 1223-1231.

Nam, Y.J. and Ooka, R., 2010, Numerical simulation of ground heat and water transfer for groundwater heat pump system based on real-scale experiment, Energy and Buildings, 42, 69-75.

Neuman, S.P., 1990, Universal scaling of hydraulic conductivities and dispersivities in geologic media, Water Resources Research, 26(8), 1749-1758.

Park, B.H., Bae, G.O., and Lee, K.K., 2015, Importance of thermal dispersivity in designing groundwater heat pump (GWHP) system: Field and numerical study, Renewable Energy, 83, 270-279.

Rau, G.C., Andersen, M.S., and Acworth, R.I., 2012, Experimental investigation of the

thermal dispersivity term and its significance in the heat transport equation for flow in sediments, *Water Resources Research*, 48, W03511.

Rau, G.C., Andersen, M.S, McCallum, G.C., Roshan, H., and Acworth, R.I., 2014, Heat as a tracer to quantify water flow in near-surface sediments, *Earth-Science Reviews*, 129, 40-58.

Schulze-Makuch, D., 2005, Longitudinal dispersivity data and implications for scaling behavior, *Groundwater*, 43(3), 443-456.

Stauffer, F., Bayer, P., Blum, P., Molina-Giraldo, N., and Kinzelbach, W., 2013, *Thermal use of shallow groundwater*, CRC Press, 287 p.

Testu, A., Didierjean, S., Maillet, D., Moyne, C., Metzger, T., and Niass, T., 2007, Thermal dispersion for water or air flow through a bed of glass beads, *International Journal of Heat and Mass Transfer*, 50(7-8), 1469-1484.

Yagi, S., Kunii, D., and Wakao, N., 1960, Studies on axial effective thermal conductivities in packed beds, *American Institute of Chemical Engineers Journal*, 6(4), 543-546.

Zhou, X., Gao, Q., Chen, X., Yu, M., and Zhao, X., 2013, Numerically simulating the thermal behaviors in groundwater wells of groundwater heat pump, *Energy*, 61, 240-247.

국문 초록

개방형 지열시스템 (GWHP)은 지하수를 열교환에 직접 이용하기 때문에, 시스템의 효율이 대수층의 수리적 및 열적 특성에 복잡하게 영향을 받는다. 개방형 지열시스템의 효율에 영향을 주는 인자를 파악하기 위해 대수층의 수리적 특성과 관정 배열에 주목한 연구는 많았던 반면, 대수층의 열적 특성에 주목한 연구는 드물었다. 그러나 최근에 빠른 지하수 유속 조건에서는 열분산 특성이 대수층의 열거동에 미치는 영향력이 증가한다는 연구결과가 있었고 이에 따라, 빠른 지하수 흐름을 야기하는 개방형 지열시스템에서 열분산의 영향력을 파악하는 연구가 필요할 것으로 생각된다. 본 연구에서는 인공적으로 유속이 빨라진 지하수 환경에서의 열분산 양상을 파악하기 위해 포화 대수층 내의 열거동을 모사할 수 있는 실내 실험 장비를 구축하였다. 연구의 주요 목적은 물의 주입으로 유속이 빨라진 지하수 환경에서의 열분산계수를 파악하고 자연 지하수 환경에서의 열분산계수와 비교하는 것이다. 이를 위해 두 종류의 열원, 소형 저항기와 온도가 다른 주입수를 이용하여 실내 규모의 열추적자 시험을 진행하였고 추가적으로 수치 모델 시뮬레이션을 수행하였다. 먼저 저항기를 열원으로 한 열추적자 시험 결과를 분석하여 학계에서 논의가 진행되고 있는 열분산계수와 지하수 유속과의 관계식을 확인하였다. 본 실험 조건 ($Pe^t < 1$)에서는 열분산계수가 지하수 유속과 선형적인 관계식을 갖는 것으로 나타났다. 이러한 관계식을 기반으로 온도가 다른 물의 주입을 활용한 열추적자 시험 및 추가 수치 모델링 결과, 같은 배경 지하수 유속 조건에서 저항기를 열원으로 한 경우 즉, 주입으로 인한 속도장의 교란이 없는 자연 지하수 환경에서보다 열분산계수가 크게 도출되었다. 자연 지하수 환경 대비 교란된 지하수 환경에서의 열분산계수 증가율은 배경 지하수 유속이 느릴수록, 주입수의 유량이 클수록 높게 나타났다. 이는 주입으로 인해 교란이 있는 지하수 환경에서는 열플룸의 거동에 열분산이

미치는 영향력이 커짐을 암시한다. 또한, 이러한 열분산의 영향력이 배경지하수 유속이 느릴수록 그리고 주입유량이 많을수록 커짐을 시사한다. 따라서 온도가 다른 물의 주입을 활용하여 지중 열실험을 진행할 때는 정확한 열분산계수의 적용이 지중 열거동 평가에 중요한 영향을 미칠 수 있다. 특히, 배경 지하수 유속이 느리고 주입유량이 큰 조건일수록 잘못된 열분산계수 입력이 열거동 평가에 상당한 오류를 야기할 수 있다.

주요어: 개방형 지열시스템, 온수 주입, 교란된 지하수 환경, 열추적자 시험, 열분산계수, 유속